

1 **Unchanged PM2.5 levels over Europe during COVID-19 were**
2 **buffered by ammonia**

3
4 **Nikolaos Evangeliou^{1*}, Ondřej Tichý², Marit Svendby Otervik¹, Sabine Eckhardt¹, Yves**
5 **Balkanski³, Didier A. Hauglustaine³**

6
7 ¹ NILU, Department for Atmospheric & Climate Research (ATMOS), 2007 Kjeller, Norway.

8 ² The Czech Academy of Sciences, Institute of Information Theory and Automation, Prague, Czech
9 Republic.

10 ³ Laboratoire des Sciences du Climat et de l'Environnement (LSCE), CEA-CNRS-UVSQ, 91191,
11 Gif-sur-Yvette, France.

12
13 * Corresponding author: N. Evangeliou (Nikolaos.Evangeliou@nilu.no)

14
15

16 **Abstract**

17 The coronavirus outbreak in 2020 had devastating impact on human life, albeit a positive effect
18 for the environment reducing emissions of primary aerosols and trace gases and improving air quality.
19 In this paper, we present inverse modelling estimates of ammonia emissions during the European
20 lockdowns of 2020 based on satellite observations. Ammonia has a strong seasonal cycle and mainly
21 originates from agriculture. We further show how changes in ammonia levels over Europe, in
22 conjunction with decreases in traffic-related atmospheric constituents modulated PM2.5. The key
23 result of this study is a -9.8% decrease in ammonia emissions in the first half of 2020 compared to
24 the same period in 2016–2019 attributed to restrictions related to the global pandemic. We further
25 calculate the delay in the evolution of the ammonia emissions in 2020 before, during and after
26 lockdowns, by a sophisticated comparison of the evolution of ammonia emissions during the same
27 time periods for the reference years (2016–2019). Our analysis demonstrates a clear delay in the
28 evolution of ammonia emissions of -77 kt, that was mainly observed in the countries that suffered the
29 strictest travel, social and working measures. Despite the general drop in emissions during the first
30 half of 2020 and the delay in the evolution of the emissions during the lockdown period, satellite and
31 ground-based observations showed that the European levels of ammonia increased. On one hand, this
32 was due to the reduction of SO_2 and NO_x (precursors of the atmospheric acids with which ammonia
33 reacts) that caused less binding and thus less chemical removal of ammonia (smaller loss – higher
34 lifetime); on the other, the majority of the emissions persisted, because ammonia mainly originates
35 from agriculture, a primary production sector that was influenced slightly by the lockdown
36 restrictions. Despite the projected drop in various atmospheric aerosols and trace gases, PM2.5 levels
37 stayed unchanged or even increased in Europe, due to a number of reasons attributed to the
38 complicated $NH_3 - H_2SO_4 - HNO_3$ system. Higher water vapour during the European lockdowns
39 favoured more sulfate production from SO_2 and OH (gas phase) or O_3 (aqueous phase). Ammonia
40 first reacted with sulfuric acid also producing sulfate. Then, the continuously accumulating free
41 ammonia reacted with nitric acid shifting the equilibrium reaction towards particulate nitrate. In high
42 free ammonia atmospheric conditions such as those in Europe during the 2020 lockdowns, a small
43 reduction of NO_x levels drives faster oxidation toward nitrate and slower deposition of total inorganic
44 nitrate causing high secondary PM2.5 levels.

45

46 **1 Introduction**

47 Ammonia (NH₃), the most abundant gas, has played a vital role in the evolution of human
48 population through the Haber–Bosch process (Chen et al., 2019). However, today it is recognized to
49 have significant negative influence, not only for the environment (Stevens et al., 2010), but also for
50 human population (Cohen et al., 2017; Pope and Dockery, 2006) and the climate (De Vries et al., 2011).
51 As an alkaline molecule, ammonia regulates the pH of clouds, while its excessive atmospheric
52 deposition and terrestrial runoff affect natural reservoirs creating algae blooms and degrading water
53 quality (Camargo and Alonso, 2006; Krupa, 2003). When emitted to the atmosphere, it reacts with
54 the abundant sulfuric and nitric acids (Malm, 2004) forming sulfate, nitrate, and ammonium and
55 contributing up to 50% to the total aerosol mass (Anderson et al., 2003). The latter has implications
56 for human health (Gu et al., 2014) as aerosols penetrate the human respiratory system and accumulate
57 in the lungs (Pope III et al., 2002) causing premature mortality (Lelieveld et al., 2015). Furthermore,
58 through secondary aerosol formation (Pozzer et al., 2017), ammonia has a significant impact (i) on
59 regional climate (Bellouin et al., 2011) causing visibility problems and contributing to haze effect,
60 and (ii) on global climate directly by scattering incoming radiation (Henze et al., 2012) and indirectly
61 as cloud condensation nuclei (Abbatt et al., 2006) altering the Earth’s radiative balance.

62 The largest portion of atmospheric ammonia originates from the synthesis of nitrogen
63 fertilizers, which are in high demand for agriculture (Erisman et al., 2007). The expansion of intensive
64 agriculture during the 20th century has increased atmospheric ammonia above natural levels (Erisman
65 et al., 2008), while the projected growth of the global population will likely create larger nutritional
66 needs that are expected to further increase ammonia emissions during the 21st century (Pai et al.,
67 2021). Other sources of ammonia include emissions from livestock (Sutton et al., 2000a), industry,
68 ammonia-rich watersheds (Sørensen et al., 2003), traffic (Kean et al., 2009), sewage (Reche et al.,
69 2012), humans (Sutton et al., 2000b), biomass and domestic combustion (Sutton et al., 2008; Fowler
70 et al., 2004) and volcanic eruptions (Sutton et al., 2008).

71 In the past years, atmospheric ammonia observations were mostly limited to ground-based
72 measurements with relatively sparse monitoring networks. This resulted in large emission
73 uncertainties in regions poorly covered by measurements (Heald et al., 2012). Today, satellite
74 products are capable to record daily ammonia column concentrations providing useful information
75 on its atmospheric abundance. Recently, Van Damme et al. (2021) analyzed Infrared Atmospheric
76 Sounding Interferometer (IASI) retrievals and showed increased ammonia levels over most of Europe
77 after 2015. Then, suddenly the COVID-19 outbreak came in 2020 creating a unique situation
78 (Baekgaard et al., 2020), which affected all segments of life in a detrimental way (Chakraborty and
79 Maity, 2020; Sohrabi et al., 2020). As a measure to inhibit further spread of the virus, authorities took

80 strict social, travel and working restrictions for months, which resulted in lower traffic-related
81 emissions and improved air quality (Bauwens et al., 2020; Dutheil et al., 2020; Sicard et al., 2020).
82 Illustrating the impact on emissions, Guevara et al. (2021) reported average emission reductions in
83 Europe to be 33% for NO_x , 8% for non-methane volatile organic compounds (NMVOCs), and 7%
84 for SO_x during the strictest lockdowns in 2020, while more than 85% of the total reduction is
85 attributed to road transport. CO_2 emissions were also decreased by 11% over Europe during the first
86 lockdowns (Diffenbaugh et al., 2020), so as aerosols did; notably Black Carbon (BC) emissions
87 dropped by 11% (Evangelidou et al., 2020) and Aerosol Optical Depth (AOD) decreased up to 20%
88 over Central and Northern Europe (Acharya et al., 2021).

89 While the COVID-19 lockdown impact on emissions for primary aerosols and trace gases has
90 been studied extensively, how ammonia emissions were affected in Europe is unknown. The latter is
91 very important and may have largely moderated the atmospheric levels of particulate matter (Giani
92 et al., 2020; Guevara et al., 2021; Matthias et al., 2021), because of ammonia's contribution to
93 secondary PM_{2.5} (particulate matter) formation (Anderson et al., 2003). Here, we make use of
94 satellite measurements of ammonia and a novel inversion algorithm to track how ammonia emissions
95 changed before, during and after the European lockdowns in 2020. We examine the reasons behind
96 the estimated changes and validate the results against ground-based observations from the EMEP
97 measurement network (<https://emep.int/mscw/>, **Figure S 1**). Finally, we calculate the resulting impact
98 of ammonia changes during the European lockdowns on the formation of PM_{2.5} using a chemistry
99 transport model (CTM) and try to interpret the mechanisms governing these changes.

100 **2 Methods**

101 **2.1 Cross-Track Infrared Sounder (CrIS) ammonia measurements**

102 The CrIS sensor onboard the NASA Suomi National Polar-orbiting Partnership provides
103 atmospheric soundings at high spectral resolution (0.625 cm^{-1}) (Shephard et al., 2015) resulting in
104 improved vertical sensitivity for ammonia at the surface (Zavyalov et al., 2013). The CrIS fast
105 physical algorithm (Shephard and Cady-Pereira, 2015) retrieves ammonia at 14 vertical levels using
106 a physics-based optimal estimation retrieval, which also provides the vertical sensitivity (averaging
107 kernels) and an estimate of the retrieval errors (error covariance matrices) for each measurement.
108 Shephard et al. (2020) reports a total column random measurement error of 10–15%, with total
109 random errors of ~30%. The individual profile random errors are 10–30%, while total profile random
110 errors increase above 60% due to the limited vertical resolution (Shephard et al., 2020). Vertical
111 sensitivity and error calculations are also important when using CrIS observations in satellite inverse
112 modelling applications (Li et al., 2019; Cao et al., 2020) as a satellite observational operator can be

113 generated in a robust manner (see next sections). The detection limit of CrIS measurements has been
114 calculated down to 0.3–0.5 ppbv (Shephard et al., 2020) and the product has been validated
115 extensively against ground-based observations (Dammers et al., 2017; Kharol et al., 2018) showing
116 small differences and high correlations.

117 Daily CrIS ammonia satellite measurements (version 1.6.2) were gridded on $0.5^\circ \times 0.5^\circ$ covering
118 all Europe (10°W – 50°E , 25°N – 75°N) from 1st January to 30th June 2020. Data were screened prior
119 to its use with Quality Flag ≥ 4 , as recommended in the CrIS documentation, and Cloud Flag $\neq 1$. The
120 latter excludes retrievals that are performed under thin cloud conditions and are not as reliable as
121 retrievals performed under cloud-free conditions (White et al., 2023). Gridding was chosen to limit
122 the large number of observations (around 10,000 per day per vertical level for 2550 retrievals January
123 to June 2020), hence the need for a large number of source-receptor matrices (SRMs), which is
124 computationally inefficient. Specifically, day and night-time observations from CrIS were averaged
125 in each 0.5° resolution grid-cell daily from 1st January to 30th June 2020. This gridding method,
126 although simple, it gives more robust results than classic interpolation methods and presents small
127 standard deviations of the gridded values (see Tichý et al., 2023). Sitwell and Shephard (2021)
128 showed that the averaging kernels of CrIS ammonia are significant only for the lowest six levels (the
129 upper eight have no influence into the satellite observations) and therefore we have considered these
130 six vertical levels (~ 1018 - 619 hPa).

131 **2.2 Source-receptor matrix (SRM) calculations**

132 SRMs were calculated for each $0.5^\circ \times 0.5^\circ$ grid-cell over Europe (10°W – 50°E , 25°N – 75°N)
133 using the Lagrangian particle dispersion model FLEXPART version 10.4 (Pisso et al., 2019) adapted
134 to model ammonia. The model releases computational particles that are tracked backward in time
135 using hourly ERA5 (Hersbach et al., 2020) assimilated meteorological analyses from the European
136 Centre for Medium-Range Weather Forecasts (ECMWF) with 137 vertical layers and a horizontal
137 resolution of $0.5^\circ \times 0.5^\circ$. FLEXPART simulates turbulence (Cassiani et al., 2015), unresolved
138 mesoscale motions (Stohl et al., 2005) and convection (Forster et al., 2007). SRMs were calculated
139 for 7 days backward in time, at temporal intervals that matched satellite measurements and at spatial
140 resolution of $0.5^\circ \times 0.5^\circ$. This 7-day backward tracking is sufficiently long to include almost all
141 ammonia sources that contribute to surface concentrations at the receptors given a typical atmospheric
142 lifetime of about a day (Evangelidou et al., 2021; Van Damme et al., 2018).

143 The complicated heterogeneous chemistry of ammonia was modelled with the Eulerian model
144 LMDz-OR-INCA, which couples the LMDz (Laboratoire de Météorologie Dynamique) General
145 Circulation Model (GCM) (Hourdin et al., 2006) with the INCA (INteraction with Chemistry and
146 Aerosols) model (Folberth et al., 2006; Hauglustaine et al., 2004) and with the land surface dynamical

147 vegetation model ORCHIDEE (ORganizing Carbon and Hydrology In Dynamic Ecosystems)
148 (Krinner et al., 2005). The model has a horizontal resolution of $2.5^{\circ} \times 1.3^{\circ}$, and 39 hybrid vertical
149 levels extending to the stratosphere. It accounts for large-scale advection of tracers (Hourdin and
150 Armengaud, 1999), deep convection (Emanuel, 1991), while turbulent mixing in the planetary
151 boundary layer (PBL) is based on a local second-order closure formalism. The model simulates
152 atmospheric transport of natural and anthropogenic aerosols and accounts for emissions, transport
153 (resolved and sub-grid scale), and dry and wet (in-cloud/below-cloud scavenging) deposition of
154 chemical species and aerosols interactively. LMDz-OR-INCA includes a full chemical scheme for
155 the ammonia cycle and nitrate particle formation, as well as a state-of-the-art
156 $\text{CH}_4/\text{NO}_x/\text{CO}/\text{NMHC}/\text{O}_3$ tropospheric photochemistry (Hauglustaine et al., 2014). The global
157 transport of ammonia was simulated for 2020 with a month of spin-up by nudging the winds of the
158 3-hourly ERA5 (Hersbach et al., 2020) with a relaxation time of 10 days (Hourdin et al., 2006).

159 For the calculation of ammonia's lifetime, LMDz-OR-INCA ran with traditional emissions for
160 anthropogenic, biomass burning and oceanic emission sources from ECLIPSEv5a (Evaluating the
161 CLimate and Air Quality ImPacts of Short-livEd Pollutants), GFED4 (Global Fire Emission Dataset)
162 and GEIA (Global Emissions InitiAtive) (hereafter called "EGG") (Bouwman et al., 1997; Giglio et
163 al., 2013; Klimont et al., 2017). FLEXPART uses the exponential mass removal for radioactive
164 species based on the e-folding lifetime (Pisso et al., 2019), which gives the time needed to reduce the
165 species mass to $1/e$ contribution. We calculated the e-folding lifetime (Kristiansen et al., 2016; Croft
166 et al., 2014) of ammonia from LMDz-OR-INCA, assuming that the loss occurs as a result of all
167 processes affecting ammonia (chemical reactions, deposition) with a minimum time-step of 1800 s.
168 Then we calculated the exponential loss of ammonia and the respective loss-rate constant κ (s^{-1}). We
169 point to Tichý et al. (2023) for more details on the methodology to avoid repetition.

170 Ammonia has a complicated atmospheric chemistry and may react with sulfuric and nitric acid
171 producing sulfate and nitrate. However, under certain atmospheric conditions, the equilibrium
172 reaction with nitric acid can be shifted to the left producing free ammonia (Seinfeld and Pandis, 2000).
173 Tichý et al. (2023) showed that production of free ammonia happened very rarely in continental
174 Europe in 2013–2020 period. Nevertheless, we have previously published a full validation of the
175 obtained CTM concentrations against all the available ground-based measurements of ammonia
176 globally (Tichý et al., 2023), from the EMEP network (<https://emep.int/mscw/>) in Europe, EANET
177 (East Asia acid deposition NETwork) in Southeastern Asia (<https://www.eanet.asia/>) and AMoN
178 (Ammonia Monitoring Network in the US, AMoN-US; National Air Pollution Surveillance Program
179 (NAPS) sites in Canada) in North America (<http://nadp.slh.wisc.edu/data/AMoN/>) .

180 2.3 Inverse modelling of ammonia emissions

181 The proposed inversion method is based on a comparison of the CrIS satellite observations with
 182 the model profile retrievals to estimate the spatiotemporal ammonia emissions. The comparison of
 183 remote-sense observations such as CrIS with model (or in-situ) profiles is not straightforward as in
 184 the cases of ground-based observations. Here, we used the more rigorous approach of the “instrument
 185 operator” (see equation below), after interpolation of the model profile to the first six levels of the
 186 satellite product (Rodgers, 2000):

$$187 \quad \ln(v^{ret}) = \ln(v^a) + A(\ln(v^{true}) - \ln(v^a)) \quad Eq. 1$$

188 where v^{ret} is the retrieved profile concentration vector, v^a is a priori profile concentration vector,
 189 v^{true} is the true profile concentration vector, and A is the averaging kernel matrix in logarithmic
 190 space (for each $0.5^\circ \times 0.5^\circ$ resolution grid-cell). In our inversion setup, we directly compared the
 191 retrieved v^{ret} and the observed satellite column concentration v^{sat} that is given by CrIS. In our case,
 192 v^{true} is equal to the modelled concentration v^{mod} calculated from the SRMs and a prior emission
 193 inventory. The argument for this approach is that v^{ret} is what the satellite would observe if v^{mod} was
 194 the true profile. This is a useful technique for evaluating if the retrieval algorithm is performing as
 195 designed, i.e., is it unbiased and the calculated root mean square error (RMSE) is within the expected
 196 variability. Further details about the algorithm and the setup can be found in Tichý et al. (2023).

197 The goal of the inversion is to iteratively update prior emissions by minimizing the distance
 198 between v^{sat} and v^{ret} by correcting the emission flux x in the term $v^{mod} = srm^{Flex}x^a$ (srm^{Flex}
 199 denotes the FLEXPART SRMs), at each grid-cell and each of the six vertical levels that are important
 200 for CrIS (Sitwell et al., 2022):

$$201 \quad \arg \min_{x^a \rightarrow x} \|v^{sat} - v^{ret}\|_2^2 \quad Eq. 2$$

202 The inverse problem is constructed for each spatial element of the computational domain.
 203 Inspired by the construction of covariance matrix in Cao et al. (2020), we consider 4° surroundings
 204 (445 km), expressed by the index set \mathbb{S} , of which the column concentrations are considered due to
 205 computational effectivity. Note that we observed low sensitivity of resulting emission estimates to
 206 this choice. Then, we can formulate the inverse problem for each spatial element as:

$$207 \quad [v_{s_i}^{sat}; s_i \in \mathbb{S}] = [v_{s_i}^{ret}; s_i \in \mathbb{S}]q^{\mathbb{S}} \quad Eq. 3$$

208 where the left side of the equation is formed by the vector with aggregated CrIS observations, vectors
 209 $v_{s_i}^{ret}$ form a block-diagonal matrix, and $q^{\mathbb{S}}$ is an unknown vector with correction coefficients for each
 210 temporal element of the emission. The inverse problem in Eq. 3 was solved using the least squares
 211 with adaptive prior covariance (LS-APC) algorithm (Tichý et al., 2016). The algorithm is based on a

212 Bayesian model which assumes that all coefficients are positive and that the abrupt changes in their
213 neighbouring values are less probable. It is shown that the method is less sensible to manual tuning
214 of regularization parameters (see sensitivity tests in Tichý et al. (2020)) than classical optimization
215 procedures, which is crucial for such a large dataset where each spatial element represents a separate
216 inverse problem.

217 A detailed description of the algorithm is given in Tichý et al. (2016). Here, we do not describe
218 the algorithm again but explain a few modifications that were necessary for this study. By estimating
219 the correction coefficients q^S for each grid-cell of the spatial domain (10°W–50°E, 25°N–75°N), we
220 can propagate the coefficients through Eq. 2 to update a priori emissions x^a in the model
221 concentration term v^{mod} . We follow Li et al. (2019) and Cao et al. (2020) to bound the ratio between
222 the prior and the posterior emissions. The lower and upper bound of this ratio is set to 0.01 and 100,
223 respectively, to omit the unrealistically low or high emissions. We consider these bounds large
224 enough to allow for new emission sources to be exposed, not presented in the prior emissions.

225 We evaluate the performance of the inversion by using three a priori emission datasets, (i) one
226 based on Van Damme et al. (2018) calculations (hereafter “VD” corresponding to VDgrlf emissions
227 from Evangeliou et al. (2021)), (ii) the ECLIPSEv6b inventory (Klimont, 2022; Klimont et al., 2017)
228 (combined with biomass burning emissions from GFEDv4 (Giglio et al., 2013)) as the most recent
229 one (denoted as “EC6G4”), and (iii) the average of four emission inventories for ammonia, except
230 for these two mentioned before, “EGG” (see previous section), and “NE” calculated from IASI
231 (Infrared Atmospheric Sounding Interferometer) observation (Evangeliou et al., 2021) (denoted as
232 “avgEENV”). To account for the spatiotemporal impact of the lockdown on the European emissions,
233 we corrected prior emission inventories of ammonia (only the bottom-up EGG, EC6G4; the top-down
234 ones are based on satellite measurements where possible changes due to COVID-19 have been
235 captured) for 2020 using adjustment factors (AFs) adopted from Doumbia et al. (2021). The same
236 was done for SO_2 and NO_x (precursors of sulfuric and nitric acid in the atmosphere) in EGG that was
237 used to calculate ammonia’s loss rates using LMDz-OR-INCA model (see section 2.2). This dataset
238 provides, for the January–August 2020 period, gridded AFs at a $0.1^\circ \times 0.1^\circ$ resolution on a daily
239 resolution for transportation (road, air and ship traffic), power generation, industry and residential
240 sectors. The quantification of AFs is based on activity data collected from different databases and
241 previously published studies. These emission AFs have been applied to the CAMS global inventory,
242 and the changes in emissions of the main pollutants have been assessed for different regions of the
243 world in the first 6 months of 2020 (Doumbia et al., 2021).

244 **Figure 1** shows the comparison of prior and posterior concentrations against independent
245 observations (observations that were not used in the inversion algorithm) from the EMEP network

246 (<https://emep.int/mscw/>, **Figure S 1**) for January–July 2020. Note that prior concentrations of
 247 ammonia result by coupling the FLEXPART SRMs with prior emissions (from VD, ECLIPSEv6b
 248 and avgEENV), while posterior concentrations by coupling the SRMs with the calculated posterior
 249 emissions. In **Figure 1** it is evident that the most accurate reconstruction of surface concentrations
 250 with respect to the EMEP observations was obtained using avgEENV as the a priori information, and
 251 therefore the results presented hereafter are based on this setup. We performed inversions for the first
 252 half of 2020 to assess the effect of lockdown measures on ammonia emissions, as well as the situation
 253 after lockdown measures were taken away (rebound period). To have a more generic view, we also
 254 performed inverse modelling calculations for the first half of each year between 2016–2019 (reference
 255 period). Then, we assess in impact of ammonia changes on aerosol formation (PM2.5), by feeding
 256 the posterior emissions to the LMDz-OR-INCA model and calculating the production of PM2.5.

257 2.4 Statistical tests

258 To evaluate the comparisons between modelled and observed concentrations of ammonia, we
 259 used the root mean squared logarithmic error (RMSLE) defined as follows:

$$260 \quad RMSE = \sqrt{\sum_{i=1}^N \frac{(C_m - C_o)^2}{N}} \quad \text{and} \quad RMSLE = \sqrt{\frac{1}{N} \sum_{i=1}^N (\log C_m - \log C_o)^2} \quad Eq. 4$$

261 where C_m and C_o are the modelled and measured ammonia concentrations and N is the total number
 262 of observations. The commonly used squared Pearson correlation coefficient (r) was also used as a
 263 measure of linear correlation between two sets of data defined as:

$$264 \quad r = \frac{\sum (C_m - \bar{C}_m)(C_o - \bar{C}_o)}{\sqrt{(\sum (C_m - \bar{C}_m)^2)(\sum (C_o - \bar{C}_o)^2)}} \quad Eq. 5$$

265 where the distance of modelled and measured ammonia concentrations from the mean (\bar{C}_m and \bar{C}_o) is
 266 computed. Finally, the standard deviation was adopted as a measure of the dispersion of modelled
 267 ammonia from the observations, which is the true value:

$$268 \quad \sigma = \sqrt{\frac{\sum (C_m - C_o)^2}{N}} \quad Eq. 6$$

269 The mean fractional bias (*MFB*) was selected as a symmetric performance indicator that gives equal
 270 weights to under- or over-estimated concentrations (minimum to maximum values range from -200%
 271 to 200%). It was used in the independent validation (validation against measurements that were
 272 excluded from the inversion, see section 3.3) of the posterior concentrations of ammonia during the
 273 European lockdowns of 2020 and is defined as:

274
$$MFB = \frac{1}{N} \frac{\sum_{i=1}^N (C_m - C_o)}{\sum_{i=1}^N \left(\frac{C_m + C_o}{2}\right)} \quad Eq. 7$$

275 For the same reason, the mean absolute error was computed normalized (*nMAE*) over the average of
 276 all the actual values (observations here), which is a widely used simple measure of error:

277
$$MAE = \frac{\sum_{i=1}^N |C_m - C_o|}{\sum_{i=1}^N C_o} \quad Eq. 8$$

278 3 Results

279 3.1 Emission changes of ammonia due to COVID-19 restrictions over Europe

280 The reason behind the selected three priors used in the inversion (EGG, EC6G4 and avgEENV)
 281 of ammonia is trifold; (i) they are based on the most recent estimates, (ii) they present different spatial
 282 distribution, and (iii) they were derived using different methodologies. More specifically, EC6G4 is
 283 based on the emission model GAINS (Klimont et al., 2017), while VD uses satellite observations
 284 combined with a box model (Evangelidou et al., 2021). As mentioned in the previous section, it is seen
 285 that the most accurate representation of surface model concentrations was achieved using the
 286 avgEENV a priori, which forces posterior concentrations closer to 1×1 line, whereas the obtained
 287 statistics are significantly better than using other priors (**Figure 1**). Therefore, the results presented
 288 below have all been obtained using avgEENV as the prior emission dataset keeping results using the
 289 other two priors in the Supplements.

290 The total prior emissions of ammonia over Europe for the inversion period (January – June),
 291 the posterior emissions for years 2016–2019 and the posterior emissions during the lockdown year
 292 2020 (January – June) are plotted in **Figure 2** (the results from inversions using EC6G4 and VD prior
 293 emissions are illustrated in **Figure S 2** and **S 3**). The total prior ammonia emitted between January
 294 and June in Europe were equal to 1061 kt (**Figure 2a**). To check whether calculated changes in 2020
 295 were due to meteorology and avoid misinterpretation of our findings, inverse calculations of ammonia
 296 were performed for the reference years 2016–2019 (January–June) using respective observations
 297 from CrIS and exactly the same set-up as the one described in section 2 (Methods). The total posterior
 298 emissions of ammonia over Europe for the reference period (2016 – 2019) were estimated to be
 299 1665±330 kt (4-y mean±SD) or 57% higher than the prior (**Figure 2b**). Finally, for January–June
 300 2020 the derived emission estimates were equal to 1568±732 kt (posterior±uncertainty) (**Figure 2c**).
 301 This is 48% higher than the prior and 6% lower than the posterior emissions of January–June 2016–
 302 2019.

303 The weekly-average evolution of prior and posterior emissions of ammonia over Europe
 304 (January to June) for 2016–2019 show a similar pattern with small year-to-year variability (**Figure**

305 2d,e), and similar temperatures (**Figure S 4**) thus insignificant impact from the prevailing
306 meteorology that would justify change in emissions due to volatilisation. The weekly posterior
307 ammonia emissions over Europe changed during the lockdown period (2020) as compared to the
308 reference years (**Figure 2f**). Satellites and national monitoring measurements of ammonia show that
309 emissions peak in spring (March) and late-summer in Europe (Van Damme et al., 2022)
310 corresponding to the two main fertilization periods (Paulot et al., 2014). Ammonia abundances are
311 however high throughout the entire spring–summer period due to agriculture associated with rising
312 temperature (Sutton et al., 2013). Ammonia posterior emissions in 2020 declined by -9.8% as
313 compared to the same period over the previous four years (2016–2019, **Figure 2f**). Although the
314 obtained posterior emissions for the reference period (dashed grey line and shade) are very similar to
315 those of 2020, (solid blue line and shade in **Figure 2f**), emissions during lockdown period in 2020
316 dropped substantially, outside of the deviation of the emissions in the reference period (**Figure 2f**).

317 **3.2 Uncertainty of the posterior emissions**

318 As described in section 2.3 in more detail, we considered 4° surroundings of each spatial
319 element of our inversion domain from which the CrIS observations were used in the inverse problem.
320 This means that 45 spatial elements in CrIS space were used, with six vertical levels each, for each
321 of the 26 temporal emission elements. To calculate the associated uncertainty of the posterior
322 estimates, we tested two sources of uncertainty: (i) how different surroundings for each spatial
323 element affect posterior emissions of ammonia and (ii) how the use of different prior emissions affects
324 posterior ammonia. We organized a series of sensitivity tests using surroundings covering 2°, 3° and
325 4° from each grid-cell. This selection is realistic as it was shown previously in Cao et al. (2020) for
326 the construction of prior emission error covariance matrix. For the second source of uncertainty, we
327 performed the same inversion using not only EC6G4 and VD priors, but also adding results using two
328 more datasets for ammonia (in total four), which have 10 times higher emissions, namely EGG and
329 NE (see section 2.3).

330 The calculated absolute uncertainties are depicted in **Figure 3a–c** together with the relative
331 uncertainty (**Figure 3d**) with respect to the posterior emissions of ammonia (posterior ammonia is
332 shown in **Figure 2c**). The first source of uncertainty (different surroundings) slightly affects the
333 resulting posterior emissions of ammonia (**Figure 3a**) causing an average relative uncertainty below
334 4% in the European emissions. The second source of uncertainty (use of different priors) causes much
335 larger bias as shown in **Figure 3b** (average relative uncertainty 35%). The reason for this is obviously
336 the large variation of the EGG (Bouwman et al., 1997; Giglio et al., 2013; Klimont et al., 2017) and
337 NE (Evangelidou et al., 2021) prior datasets that have total emissions in the first half of 2020 of 63.5
338 and 53.3 Tg, respectively, in contrast to only 6.2 and 5.7 Tg for EC6G4 and VD. Hence, the results
339 presented here are sensitive to the use of prior emission dataset. The modelled concentrations (that

340 replaces the hypothetical true column concentration in Eq. 1) is calculated by the SRMs and the prior
341 emission and, therefore, play a key role in the comparison of the CrIS value (v^{sat}) and retrieved value
342 (v^{ret}) (see Eq. 2). Also, the modelled concentrations stand as the argument of the natural logarithm
343 weighted by the averaging kernel in logarithmic space. The linearization of this operator as suggested
344 by Sitwell and Shephard (2021) may reduce the dependency on the prior emission term, however,
345 this is beyond the scope of this study. Overall, the propagated (absolute and relative) uncertainties of
346 the posterior emissions are shown in **Figure 3c** and d and are equal to 66% over Europe on average
347 (**Figure 3**). The latter shows that our calculations are robust on one hand, but dependent on the use
348 of a priori information on the other.

349 **3.3 Validation of posterior ammonia against independent measurements**

350 The optimized emissions of ammonia must be validated against independent observations,
351 because the inversion algorithm has been designed to reduce the model–observation mismatches.
352 Here, the reduction of the posterior concentration differences from the observations from CrIS is
353 determined by the weighting that is given to the observations and, hence, such comparison depends
354 on this weighting (dependent observations). Therefore, the ideal comparison of any posterior
355 emission resulting from top-down methods would be against measurements that were not included in
356 the inversion algorithm (independent observations). Here, we used ground-based observations of
357 ammonia from all EMEP sites (<https://emep.int/mscw/>) for the period of our study as an independent
358 dataset for validation. All stations are illustrated in **Figure S 1**.

359 As we mentioned in section 2.3, we evaluated the efficiency of the inversion and the most
360 effective a priori dataset for our purpose by assessing the match between the calculated posterior
361 concentrations against all the available observations from EMEP (N=3957) for the study period
362 (**Figure 1**). More specifically, after it became evident that the most accurate results were obtained
363 with avgEENV as the prior (relationship closer to unity against measured ammonia), we saw an
364 immediate improvement in the statistical tests used (nRMSE, nMAE and RMSLE) when using the
365 posterior emissions to model ammonia in FLEXPART during the first half of 2020 (**Figure 1** – right
366 panel). nMAE decreased from 0.80 using the prior emissions to 0.76 using the posterior ones,
367 accordingly nRMSE of the posterior concentrations dropped to 0.073 as compared to -0.069 using
368 the prior emissions, while the RMSLE decreased from 0.60 using prior emissions to 0.55 using the
369 optimized a posteriori emissions. To get a better insight on how modelled concentrations improved
370 towards ammonia observations, eight random EMEP stations were selected to show timeseries of
371 prior and posterior concentrations in the first half of 2020 (**Figure S 5**). Although large peaks were
372 not reproduced, all statistics were improved using the posterior emissions of ammonia.

373 3.4 Country-level changes due to COVID-19 restrictions

374 To document the emission changes of ammonia over the different European countries before,
375 during and after the 2020 lockdowns, we report the weekly evolution of the emissions for 16 countries
376 individually (**Figure 4**). Specifically, weekly emissions were averaged for each country based on
377 respective country definitions that are shown in **Figure S 6** using the avgEENV prior.

378 Most countries show that ammonia emissions declined or at least stayed less affected by the
379 2020 lockdowns, as compared to the same period during the reference years (2016–2019). Countries
380 with substantial decreases in the 2020 lockdown emissions were The Netherlands (-16%) and
381 Belgium (-23%), both countries with important agricultural activity, as well as Denmark (-20%),
382 Ireland (-18%) and Ukraine (-18%). Smaller changes were recorded in Spain (-2.1%), Czechia (-
383 4.0%) and Italy (-6.0%) despite the intensive lockdown measures. This practically shows that
384 agricultural activity is insignificantly affected, even in periods of extraordinary austerity, as the last
385 remaining primary production sector, necessary for human life.

386 We note that the largest emissions of ammonia in European countries were seen around
387 March–April (weeks 8–16) and in summer. These coincide with the fertilization periods mentioned
388 previously (Paulot et al., 2014) that control the seasonality of ammonia's emissions. In most European
389 countries, the time of the year when fertilizers can be applied is tightly regulated (Ge et al., 2020). In
390 the Netherlands and Belgium, for instance, the largest ammonia contributing region in Europe,
391 application of nitrogen fertilizer is only allowed from February to mid-September. This produces two
392 peak periods, in March and late May (**Figure 4**). Manure application also follows stringent
393 regulations and is only allowed in the same periods depending on the type of manure (slurry or solid)
394 and the type of land (grassland or arable land) (Van Damme et al., 2022).

395 To understand and position where ammonia emissions changed during the European
396 lockdowns of 2020, we plot the difference of the posterior emissions of ammonia during the lockdown
397 period (15 March – 30 April) for the same period in **Figure 5a**. We calculate higher emissions of
398 ammonia during the lockdown of +115 kt as compared to the prior emissions. Note that inversion
399 algorithms aim at reducing the mismatches between modelled concentrations and observations (in
400 our case, from CrIS satellite measurements) by correcting emissions. This means that different
401 posterior emissions are most likely, due to errors in the prior emissions and do not indicate any impact
402 from the restriction measures.

403 Therefore, we demonstrate the impact of the COVID-19 lockdowns over Europe in 2020, by
404 calculating the emission anomaly for the lockdown period from 2016–2020 (same period as the 2020
405 lockdowns, namely 15 March – 30 April) in **Figure 5b**. Emissions during the 2020 lockdowns

406 dropped by -29 kt with respect to the same period in 2016 – 2020 showing the impact of the COVID-
407 19 restrictions. Maximum decreases were seen in The Netherlands and Belgium, both countries
408 comprising high emissions (**Figure 5b**) that also suffered heavily from the COVID-19 outbreak
409 (Bendz and Aaberge, 2020) and took strict lockdown measures. Other areas where significant changes
410 were calculated were Northern Italy, Switzerland and Austria, while Scandinavian countries were not
411 affected. This agrees well with the state of the epidemic in these countries in spring 2020. While
412 North Italy was the first country outside China to suffer high mortality rates and, thus, dramatic social
413 restrictions in spring 2020, Norway, Sweden, Denmark and Finland showed total infected cases far
414 below 1% per capita, mostly suffering higher rates later in 2020 (Gordon et al., 2021).

415 As mentioned previously, ammonia emissions increase in spring (March) and late-summer in
416 Europe (Van Damme et al., 2022; Paulot et al., 2014). Therefore, calculating the difference in the
417 calculated emissions during the lockdown from the period before or after is practically meaningless
418 and cannot show the lockdown impact since agricultural activity was slightly affected in 2020. For
419 this reason we quantify the delay in the evolution of the 2020 emissions by calculating emission
420 differences in the lockdowns from the period before (Lock – Prelock) for the lockdown year 2020
421 and emission differences (Lock – Prelock) for the reference years (2016 – 2019). Then, we plot their
422 spatial differences in **Figure 5c**. Accordingly, we do the same calculation for differences in the
423 rebound period (the period after the restrictions were relaxed) from the lockdown period (Rebound –
424 Lock) in 2020 and compare them with Rebound – Lock for the reference years 2016 – 2019 (**Figure**
425 **5d**). We observe a clear delay in the evolution of ammonia emissions in 2020 of -77 kt (**Figure 5c**),
426 while only Scandinavian countries show positive changes. Hot-spots of negative evolution were seen
427 in central Europe, mainly in the triptych of Northern Italy, Switzerland and Austria, for the reasons
428 discussed in the previous paragraph. In Poland, social measures affected the daily lives of citizens
429 significantly (Szczepańska and Pietrzyka, 2021) and might be the reason for the decreased evolution
430 of ammonia emissions (**Figure 5c**). After the measures were relaxed, the evolution of the emissions
431 rebounded slightly with respect to the reference period (2016 – 2019) as shown in **Figure 5d**. The
432 changes in ammonia during the rebound period were concentrated in countries that were affected
433 most severely from the lockdown restrictions, namely Northern Italy, Switzerland, Austria and
434 Poland. The same has been reported elsewhere for several other pollutant emissions (Davis et al.,
435 2022; Jackson et al., 2022).

436 4 Discussion

437 4.1 Rising ammonia concentrations during the European lockdowns

438 One issue that has been overlooked is the concentrations of ammonia before, during and after
439 the 2020 lockdowns in Europe. Despite the delay in the emissions during the lockdown period in
440 2020 (section 3.4), satellite ammonia from CrIS showed an increase during the lockdowns and
441 declined after the restrictions were relaxed in almost all European countries (**Figure 4**). The latter
442 was reported in several studies analysing ground-based measurements. For example, Lovarelli et al.
443 (2021) concluded that contrary to other air pollutants, ammonia was not reduced, when the COVID-
444 19 restrictions were introduced in North Italy. They further reported that urban and rural ammonia
445 was the highest compared to previous years during the same months for which the strictest lockdowns
446 occurred (i.e., spring 2020). Rennie et al. (2020) reported a slight decrease of ammonia in the UK,
447 while Xu et al. (2022) observed increased of ambient ammonia during the lockdowns in China.
448 Accordingly, Viatte et al. (2021) found enhanced ammonia during lockdown in Paris. Finally, in a
449 recent study, Kuttippurath et al. (2023) reported increase in ammonia during lockdowns almost
450 everywhere, with maxima in Western Europe, Eastern China, the Indian subcontinent and the Eastern
451 USA. Since atmospheric ammonia has been increasing globally due to various anthropogenic
452 activities, the European lockdowns in 2020 offer a unique opportunity to expose ammonia's sources
453 and address the importance of secondary PM_{2.5} formation.

454 **Figure 6a** depicts the modelled atmospheric lifetime of ammonia and its dependence from the
455 calculated loss-rates over Europe for the first half of 2020. Ammonia is a particularly interesting
456 substance due to its affinity to react with atmospheric sulfuric and nitric acids producing secondary
457 aerosols. However, the reaction with sulfuric acid is more prevalent due to several factors. For
458 instance, sulfuric acid is a stronger acid than nitric acid, leading to more efficient reactions with
459 ammonia (higher reaction rate constant for ammonia with sulfuric than with nitric acid, thus faster
460 formation of ammonium sulfate) (Behera and Sharma, 2012). Furthermore, ammonium sulfate (final
461 product of ammonia reaction with sulfuric acid) is less volatile and more thermodynamically stable
462 than ammonium nitrate (product of the reaction with nitric acid) favoring the formation and
463 persistence of ammonium sulfate particles in the atmosphere (Walters et al., 2019). Finally, sulfuric
464 acid forms more stable clusters with ammonia, even in the presence of nitric acid (Liu et al., 2018).
465 Results from laboratory and field studies have confirmed that ammonia actually promotes the
466 nucleation of sulfuric acid in the atmosphere (Weber et al., 1999; Schobesberger et al., 2015). The
467 CLOUD (Cosmics Leaving Outdoor Droplets) experiment has also highlighted that ammonia
468 preferentially reacts with sulfuric acid in the atmosphere due to its strong acidity, ability to drive
469 stable aerosol formation, and significant nucleation enhancement effects (Kirkby et al., 2016; Wang

470 et al., 2022). Nitric acid plays a secondary role, primarily forming ammonium nitrate once sulfuric
471 acid has reacted, but its contribution is limited by its volatility.

472 During the lockdown period over Europe, transport and industrial activities mostly stopped,
473 and consequently the related emissions also decreased. This had an immediate effect on SO_2 and NO_x
474 (Guevara et al., 2021; Doumbia et al., 2021). Reductions of SO_2 and NO_x caused less production of
475 atmospheric sulfuric and nitric acids. The latter had a rapid twofold effect on the lifetime of ammonia:
476 (i) Less available atmospheric acids needed less ammonia for reaction towards sulfate (mainly) and
477 nitrate aerosols (secondarily) and therefore the loss-rates declined (**Figure 6a**) leading to
478 accumulation of ammonia in its free form; (ii) ammonia originates mainly from agriculture and
479 livestock, and these activities were slightly affected during the European lockdowns increasing the
480 associated emissions (see **Figure 2**, though with a lower trend than previous years as discussed in
481 section 3.4). The rising levels of ammonia during the COVID-19 lockdowns in Europe have been
482 confirmed by the CrIS observations (**Figure 2 and 3**) and have been also reported elsewhere
483 (Kuttippurath et al., 2023; Viatte et al., 2021; Xu et al., 2022; Lovarelli et al., 2021).

484 **4.2 Disturbance in the secondary formation of PM_{2.5}**

485 The response of the restriction measures on PM_{2.5} mass concentrations suggests a
486 relationship that is more complex than expected and beyond road traffic intensity, at least for Europe.
487 It has been reported that there was no systematic decrease in PM_{2.5} concentrations during COVID-
488 19 lockdowns in the USA (Archer et al., 2020; Bekbulat et al., 2021) or even in Chinese cities (Mo
489 et al., 2021), where primary sources are abundant and stringent lockdown measures decreased PM
490 levels (Zhang et al., 2023). In a recent study focusing on PM_{2.5} measurements over 30 urban and
491 regional background European sites, Putaud et al. (2023) showed that the implementation of the
492 lockdown measures resulted in minor increases in PM_{2.5} mass concentration in Europe of $+5\pm 33\%$.
493 The latter aligns well with several regional studies focusing on the impact of lockdowns to regional
494 pollution (Querol et al., 2021; Shi et al., 2021; Viatte et al., 2021; Thunis et al., 2021; Putaud et al.,
495 2021).

496 **Figure 6b** demonstrates observed PM_{2.5} from the EMEP stations (78 sites) in comparison
497 with modelled PM_{2.5} concentrations, both averaged for all sites. In modelled PM_{2.5} mass
498 concentrations, we have separated primary and secondary PM_{2.5}, as secondary PM_{2.5} is modulated
499 by the chemical state of the atmosphere as defined by the abundance in acids and free ammonia. We
500 see that observed and modelled PM_{2.5} concentrations are in good agreement in the first half of 2020.
501 The good agreement between modelled and observed concentrations can be also confirmed for most
502 of the EMEP stations over Europe with high Pearson's coefficients, low RMSE's and low standard
503 deviations in the Taylor plot that is demonstrated in **Figure S 7**. Furthermore, while secondary PM_{2.5}
504 constitute around 20-30% of the total PM_{2.5} (Dat et al., 2024; Bressi et al., 2013; Li et al., 2023), this

505 proportion increased during the European lockdowns despite that reactions of ammonia to form
506 PM_{2.5} were decelerated (as seen by the declined loss in **Figure 6a**).

507 Leung et al. (2020) reported that the abatement of nitrate in China is buffered not only by
508 increased oxidant build-up, but also by an increase in free ammonia concentrations through sulfate
509 concentration reduction, which favours ammonium nitrate formation. During COVID-19 restrictions
510 in Europe, a significant decrease of NO_x (and SO_2) emissions occurred (Guevara et al., 2021) also
511 confirmed by Doumbia et al. (2021). Thunis et al. (2021) showed that the latter might have increased
512 the oxidative capacity of the atmosphere and, in turn, PM_{2.5} formation. This is the main reason why
513 PM_{2.5} concentrations were not decreased during the COVID-19 lockdowns in many European cities
514 (Varotsos et al., 2021; Shi et al., 2021), while the same has been reported elsewhere (Huang et al.,
515 2021; Le et al., 2020; Zhang et al., 2022).

516 PM_{2.5} increased at areas less affected by primary emissions during the 2020 lockdown or at
517 areas where the oxidative atmosphere favours secondary aerosol formation. For instance, reductions
518 in PM_{2.5} were observed to be less pronounced than those in nitrogen dioxide in several regions (Patel
519 et al., 2020; Shi and Brasseur, 2020), while PM_{2.5} even increased in others (Wang et al., 2020; Li et
520 al., 2020). Li et al. (2020) indicated that while primary emissions dropped by 15–61% in China, daily
521 average PM_{2.5} concentrations were still very high (15–79 $\mu\text{g m}^{-3}$) showing that background and
522 residual pollutants were important. In a similar manner, an extreme PM_{2.5} pollution event during the
523 Chinese lockdown in Nanning that cause public concern was due to secondary aerosol formation (Mo
524 et al., 2021).

525 Here we aim at interpreting the mechanism below this disturbance in PM_{2.5} formation. As
526 explained in Seinfeld and Pandis (2000) and represented in the LMDZ-INCA model (Hauglustaine
527 et al., 2014), the neutralisation of atmospheric acids by ammonia in the atmosphere occurs through
528 ammonium sulfate formation. Sulfate ($SO_4^{2-}(s)$) is also produced from sulfur dioxide ($SO_2(g)$) gas
529 phase oxidation by the hydroxyl radical (OH). Note that the hydroxyl radical is mostly formed in the
530 atmosphere when ultraviolet radiation (UV) photolyses ozone in the presence of water vapour, hence
531 it is linked to humidity (**Figure S 8**). Sulfate production can also occur in the aqueous phase (Hoyle
532 et al., 2016) through sulfur dioxide ($SO_2(aq)$) oxidation with ozone ($O_3(aq)$) or hydrogen peroxide
533 ($H_2O_2(aq)$). In both phases, a higher humidity favors sulfate formation (**Figure S 8**). Ammonia also
534 reacts with nitric acid ($HNO_3(g)$) to form ammonium nitrate ($NO_3^-(s)$) in an equilibrium reaction. In
535 that case, as SO_2 is strongly decreased due to the restrictions (Doumbia et al., 2021) and more free
536 ammonia accumulates (see previous section), these higher gaseous ammonia levels increase the
537 particulate nitrate formation. This mechanism has been highlighted in China as an unintended
538 consequence of the of NO_x and SO_2 regulation on the PM_{2.5} levels (Lachatre et al., 2019).

539 Conducting specific experiment in the frame of the CLOUD collaboration, Wang et al. (2022)
540 reported that the $NH_3 - H_2SO_4 - HNO_3$ system forms particles synergistically, at rates orders of
541 magnitude faster than those the individual reactions of ammonia with sulfuric or nitric acid can give.
542 In addition to this mechanism, as the fraction of the total inorganic nitrate, as particulate $NO_3^-_{(s)}$
543 (instead of gaseous $HNO_3_{(g)}$), increases, and as NO_x and SO_2 decrease, while NH_3 emissions remain
544 high, a small increase in the particulate fraction greatly slows down deposition of total inorganic
545 $NO_3^-_{(s)}$ and hence drives particulate $NO_3^-_{(s)}$ to increase (Zhai et al., 2021). Thus, although NO_x
546 emissions decreased during COVID-19 lockdowns in Europe, secondary PM_{2.5} stayed unchanged,
547 because NO_x emissions reduction drives faster oxidation of NO_x and slower deposition of total
548 inorganic $NO_3^-_{(s)}$.

549 **5 Conclusion**

550 We have examined the impact of lockdown measures in Europe due to COVID-19 on the
551 atmospheric levels and emissions of ammonia using high-resolution satellite observations combined
552 with a dispersion model and an inverse modelling algorithm. We find that ammonia emissions in
553 2020 declined by -9.8% as compared to the same period in previous years (2016–2019). However,
554 this decrease is insensitive to the meteorological conditions, as the 2020 ammonia emissions during
555 the European lockdowns dropped outside of the deviation of the emissions in the reference period
556 (2016–2019), while temperature, humidity and precipitation showed limited variability.

557 While ammonia emissions generally increase in spring and late summer in Europe due to
558 fertilisation, during the 2020 lockdowns, a clear delay in the evolution of the emissions of -77 kt was
559 calculated, mostly in the central European countries, which suffered by the stringent restrictions. The
560 evolution of ammonia emissions slightly rebounded after the restrictions were relaxed.

561 During the COVID-19 lockdowns of 2020 over Europe the atmospheric levels of ammonia
562 were drastically increased, as confirmed by ground-based and satellite observations. The reason for
563 this is twofold; first, the European lockdown measures reduced atmospheric emissions and levels of
564 SO_2 and NO_x and their acidic products (H_2SO_4 and HNO_3) slowing down binding and chemical
565 removal of ammonia (lifetimes increased), and thus accumulating free ammonia; second, the prevail
566 of agricultural activity during the lockdowns increased ammonia emissions (though at a lower rate).

567 Surprisingly, despite all the travel, working and social restrictions that the European
568 governments took to combat the outbreak of COVID-19, ambient pollution levels did not change as
569 expected. PM_{2.5} levels were modulated by the chemical state of the atmosphere through secondary
570 aerosol formation. Secondary PM_{2.5} rather increased during the European lockdowns despite that the

571 precursors of H_2SO_4 and HNO_3 declined. More sulfate was produced from SO_2 and OH (gas phase)
572 or O_3 (aqueous phase), while both atmospheric reactions were favoured by higher water vapour
573 (humidity) during the lockdown period. The accumulated ammonia reacted with H_2SO_4 first
574 producing sulfate. Then, as SO_2 decreased during the European lockdowns and more free ammonia
575 accumulated, the high excess gaseous ammonia reacted with HNO_3 shifting the equilibrium reaction
576 towards conversion to particulate nitrate causing unintended increase in the PM2.5 levels. While NO_x
577 emissions declined during the European lockdowns by -33%, this reduction drives faster oxidation of
578 NO_x and slower deposition of total inorganic nitrate causing high secondary PM2.5 levels.

579 The present study gives a comprehensive analysis of the atmospheric $NH_3 - H_2SO_4 - HNO_3$
580 system. It also proves the complicated relationship of secondary PM2.5 formation with the abundant
581 atmospheric gases. The general drop of emissions during the first consistent lockdowns of 2020 in
582 Europe offers a unique opportunity to study atmospheric chemistry under extreme conditions of fast
583 pollutant emission drop equivalent to “The Clean Air Action” of the Chinese government.

584

585 **Data availability.** All data from this study are available for download from
586 <https://datadryad.org/stash/share/Wgbc9UiXwtMH44366myWh2bt7MQc92JKhJBz7UwQlgY>
587 (reserved doi: 10.5061/dryad.12jm63z1q). The EMEP measurements of ammonia can be downloaded
588 from <https://ebas.nilu.no>. The remote sensing data for ammonia can be retrieved from
589 https://hpfx.collab.science.gc.ca/~mas001/satellite_ext/cris/snpp/nh3/v1_6_4/ or upon request to Dr.
590 M. W. Shephard. FLEXPART version 10.4 model can be downloaded from <https://www.flexpart.eu>.

591

592 **Supplement.** The supplement related to this article is available online at.

593

594 **Author contributions.** NE led the overall study, analysed the results and wrote the paper. OT
595 developed the inverse modelling algorithm and performed the inversions. MSO processed CrIS
596 ammonia on a grid. SE developed FLEXPART version 10.4 model to account for the loss of ammonia
597 from the chemistry transport model LMDz-OR-INCA. YB and DH set up and ran the chemistry
598 transport model LMDz-OR-INCA. All authors contributed to the final version of the manuscript.

599

600 **Competing interests.** The authors declare no competing interests.

601

602 **Financial support.** The work was supported by the COMBAT (Quantification of Global Ammonia
603 Sources constrained by a Bayesian Inversion Technique) project funded by ROMFORSK – Program
604 for romforskning of the Research Council of Norway (Project ID: 275407, website:

605 [https://prosjektbanken.forskingsradet.no/project/FORISS/275407?Kilde=FORISS&distribution=A](https://prosjektbanken.forskingsradet.no/project/FORISS/275407?Kilde=FORISS&distribution=A&chart=bar&calcType=funding&Sprak=no&sortBy=date&sortOrder=desc&resultCount=30&offset=0&ProgAkt.3=ROMFORSK-Program+for+romforskning)
606 [r&chart=bar&calcType=funding&Sprak=no&sortBy=date&sortOrder=desc&resultCount=30&offse](https://prosjektbanken.forskingsradet.no/project/FORISS/275407?Kilde=FORISS&distribution=A&chart=bar&calcType=funding&Sprak=no&sortBy=date&sortOrder=desc&resultCount=30&offset=0&ProgAkt.3=ROMFORSK-Program+for+romforskning)
607 [t=0&ProgAkt.3=ROMFORSK-Program+for+romforskning](https://prosjektbanken.forskingsradet.no/project/FORISS/275407?Kilde=FORISS&distribution=A&chart=bar&calcType=funding&Sprak=no&sortBy=date&sortOrder=desc&resultCount=30&offset=0&ProgAkt.3=ROMFORSK-Program+for+romforskning)). Dr. Ondřej Tichý was supported by the
608 Czech Science Foundation, grant no. GA24-10400S.

609

610 **References**

- 611 Abbatt, J. P. D., Benz, S., Cziczo, D. J., Kanji, Z., Lohmann, U., and Mohler, O.: Solid Ammonium
612 Sulfate Aerosols as Ice Nuclei: A Pathway for Cirrus Cloud Formation, *Science* (80-.), 313, 1770–
613 1773, 2006.
- 614 Acharya, P., Barik, G., Gayen, B. K., Bar, S., Maiti, A., Sarkar, A., Ghosh, S., De, S. K., and
615 Sreelesh, S.: Revisiting the levels of Aerosol Optical Depth in south-southeast Asia, Europe and
616 USA amid the COVID-19 pandemic using satellite observations, *Environ. Res.*, 193, 110514,
617 <https://doi.org/10.1016/j.envres.2020.110514>, 2021.
- 618 Anderson, N., Strader, R., and Davidson, C.: Airborne reduced nitrogen: Ammonia emissions from
619 agriculture and other sources, *Environ. Int.*, 29, 277–286, [https://doi.org/10.1016/S0160-](https://doi.org/10.1016/S0160-4120(02)00186-1)
620 [4120\(02\)00186-1](https://doi.org/10.1016/S0160-4120(02)00186-1), 2003.
- 621 Archer, C. L., Cervone, G., Golbazi, M., Al Fahel, N., and Hultquist, C.: Changes in air quality and
622 human mobility in the USA during the COVID-19 pandemic, *Bull. Atmos. Sci. Technol.*, 1, 491–
623 514, <https://doi.org/10.1007/s42865-020-00019-0>, 2020.
- 624 Baekgaard, M., Christensen, J., Madsen, J. K., and Mikkelsen, K. S.: Rallying around the flag in
625 times of COVID-19: Societal lockdown and trust in democratic institutions, *J. Behav. Public Adm.*,
626 3, 1–12, <https://doi.org/10.30636/jbpa.32.172>, 2020.
- 627 Bauwens, M., Compernelle, S., Stavrakou, T., Müller, J. F., van Gent, J., Eskes, H., Levelt, P. F.,
628 van der A, R., Veefkind, J. P., Vlietinck, J., Yu, H., and Zehner, C.: Impact of Coronavirus
629 Outbreak on NO₂ Pollution Assessed Using TROPOMI and OMI Observations, *Geophys. Res.*
630 *Lett.*, 47, 1–9, <https://doi.org/10.1029/2020GL087978>, 2020.
- 631 Behera, S. N. and Sharma, M.: Transformation of atmospheric ammonia and acid gases into
632 components of PM_{2.5}: An environmental chamber study, *Environ. Sci. Pollut. Res.*, 19, 1187–1197,
633 <https://doi.org/10.1007/s11356-011-0635-9>, 2012.
- 634 Bekbulat, B., Apte, J. S., Millet, D. B., Robinson, A. L., Wells, K. C., Presto, A. A., and Marshall,
635 J. D.: Changes in criteria air pollution levels in the US before, during, and after Covid-19 stay-at-
636 home orders: Evidence from regulatory monitors, *Sci. Total Environ.*, 769, 144693,
637 <https://doi.org/10.1016/j.scitotenv.2020.144693>, 2021.
- 638 Bellouin, N., Rae, J., Jones, A., Johnson, C., Haywood, J., and Boucher, O.: Aerosol forcing in the
639 Climate Model Intercomparison Project (CMIP5) simulations by HadGEM2-ES and the role of

640 ammonium nitrate, *J. Geophys. Res. Atmos.*, 116, 1–25, <https://doi.org/10.1029/2011JD016074>,
641 2011.

642 Bendz, B. and Aaberge, L.: COVID-19 spread in the UK: the end of the beginning?, *Lancet*, 396,
643 587–590, [https://doi.org/https://doi.org/10.1016/S0140-6736\(20\)31689-5](https://doi.org/https://doi.org/10.1016/S0140-6736(20)31689-5) www.thelancet.com,
644 2020.

645 Bouwman, A. F., Lee, D. S., Asman, W. A. H., Dentener, F. J., Van Der Hoek, K. W., and Olivier,
646 J. G. J.: A global high-resolution emission inventory for ammonia, *Global Biogeochem. Cycles*, 11,
647 561–587, <https://doi.org/10.1029/97GB02266>, 1997.

648 Bressi, M., Sciare, J., Ghersi, V., Bonnaire, N., Nicolas, J. B., Petit, J. E., Moukhtar, S., Rosso, A.,
649 Mihalopoulos, N., and Féron, A.: A one-year comprehensive chemical characterisation of fine
650 aerosol (PM_{2.5}) at urban, suburban and rural background sites in the region of Paris (France),
651 *Atmos. Chem. Phys.*, 13, 7825–7844, <https://doi.org/10.5194/acp-13-7825-2013>, 2013.

652 Camargo, J. A. and Alonso, Á.: Ecological and toxicological effects of inorganic nitrogen pollution
653 in aquatic ecosystems: A global assessment, *Environ. Int.*, 32, 831–849,
654 <https://doi.org/10.1016/j.envint.2006.05.002>, 2006.

655 Cao, H., Henze, D. K., Shephard, M. W., Dammers, E., Cady-Pereira, K., Alvarado, M., Lonsdale,
656 C., Luo, G., Yu, F., Zhu, L., Danielson, C. G., and Edgerton, E. S.: Inverse modeling of NH₃
657 sources using CrIS remote sensing measurements, *Environ. Res. Lett.*, 15, 104082,
658 <https://doi.org/10.1088/1748-9326/abb5cc>, 2020.

659 Cassiani, M., Stohl, A., and Brioude, J.: Lagrangian Stochastic Modelling of Dispersion in the
660 Convective Boundary Layer with Skewed Turbulence Conditions and a Vertical Density Gradient:
661 Formulation and Implementation in the FLEXPART Model, *Boundary-Layer Meteorol.*, 154, 367–
662 390, <https://doi.org/10.1007/s10546-014-9976-5>, 2015.

663 Chakraborty, I. and Maity, P.: COVID-19 outbreak: Migration, effects on society, global
664 environment and prevention, *Sci. Total Environ.*, 728, 138882,
665 <https://doi.org/10.1016/j.scitotenv.2020.138882>, 2020.

666 Chen, S., Perathoner, S., Ampelli, C., and Centi, G.: Chapter 2 - Electrochemical Dinitrogen
667 Activation: To Find a Sustainable Way to Produce Ammonia, in: *Horizons in Sustainable Industrial*
668 *Chemistry and Catalysis*, vol. 178, edited by: Albonetti, S., Perathoner, S., and Quadrelli, E. A. B.
669 T.-S. in S. S. and C., Elsevier, 31–46, [https://doi.org/https://doi.org/10.1016/B978-0-444-64127-](https://doi.org/https://doi.org/10.1016/B978-0-444-64127-4.00002-1)
670 [4.00002-1](https://doi.org/https://doi.org/10.1016/B978-0-444-64127-4.00002-1), 2019.

671 Cohen, A. J., Brauer, M., Burnett, R., Anderson, H. R., Frostad, J., Estep, K., Balakrishnan, K.,
672 Brunekreef, B., Dandona, L., Dandona, R., Feigin, V., Freedman, G., Hubbell, B., Jobling, A., Kan,
673 H., Knibbs, L., Liu, Y., Martin, R., Morawska, L., Pope, C. A., Shin, H., Straif, K., Shaddick, G.,
674 Thomas, M., van Dingenen, R., van Donkelaar, A., Vos, T., Murray, C. J. L., and Forouzanfar, M.

675 H.: Estimates and 25-year trends of the global burden of disease attributable to ambient air
676 pollution: an analysis of data from the Global Burden of Diseases Study 2015, *Lancet*, 389, 1907–
677 1918, [https://doi.org/10.1016/S0140-6736\(17\)30505-6](https://doi.org/10.1016/S0140-6736(17)30505-6), 2017.

678 Croft, B., Pierce, J. R., and Martin, R. V.: Interpreting aerosol lifetimes using the GEOS-Chem
679 model and constraints from radionuclide measurements, *Atmos. Chem. Phys.*, 14, 4313–4325,
680 <https://doi.org/10.5194/acp-14-4313-2014>, 2014.

681 Van Damme, M., Clarisse, L., Whitburn, S., Hadji-Lazaro, J., Hurtmans, D., Clerbaux, C., and
682 Coheur, P. F.: Industrial and agricultural ammonia point sources exposed, *Nature*, 564, 99–103,
683 <https://doi.org/10.1038/s41586-018-0747-1>, 2018.

684 Van Damme, M., Clarisse, L., Franco, B., Sutton, M. A., Erismann, J. W., Wichink Kruit, R., Van
685 Zanten, M., Whitburn, S., Hadji-Lazaro, J., Hurtmans, D., Clerbaux, C., and Coheur, P. F.:
686 Global, regional and national trends of atmospheric ammonia derived from a decadal (2008–2018)
687 satellite record, *Environ. Res. Lett.*, 16, <https://doi.org/10.1088/1748-9326/abd5e0>, 2021.

688 Van Damme, M., Clarisse, L., Stavrakou, T., Wichink Kruit, R., Sellekaerts, L., Viatte, C.,
689 Clerbaux, C., and Coheur, P. F.: On the weekly cycle of atmospheric ammonia over European
690 agricultural hotspots, *Sci. Rep.*, 12, 1–9, <https://doi.org/10.1038/s41598-022-15836-w>, 2022.

691 Dammers, E., Shephard, M. W., Palm, M., Cady-pereira, K., Capps, S., Lutsch, E., Strong, K.,
692 Hannigan, J. W., Ortega, I., Toon, G. C., Stremme, W., and Grutter, M.: Validation of the CrIS fast
693 physical NH₃ retrieval with ground-based FTIR, *Atmos. Meas. Tech.*, 87, 2645–2667, 2017.

694 Dat, N. Q., Ly, B. T., Nghiem, T. D., Nguyen, T. T. H., Sekiguchi, K., Huyen, T. T., Vinh, T. H.,
695 and Tien, L. Q.: Influence of Secondary Inorganic Aerosol on the Concentrations of PM_{2.5} and
696 PM_{0.1} during Air Pollution Episodes in Hanoi, Vietnam, *Aerosol Air Qual. Res.*, 24,
697 <https://doi.org/10.4209/aaqr.220446>, 2024.

698 Davis, S. J., Liu, Z., Deng, Z., Zhu, B., Ke, P., Sun, T., Guo, R., Hong, C., Zheng, B., Wang, Y.,
699 Boucher, O., Gentine, P., and Ciais, P.: Emissions rebound from the COVID-19 pandemic, *Nat.*
700 *Clim. Chang.*, 12, 410–417, <https://doi.org/10.1038/s41558-022-01351-3>, 2022.

701 Diffenbaugh, N. S., Field, C. B., Appel, E. A., Azevedo, I. L., Baldocchi, D. D., Burke, M., Burney,
702 J. A., Ciais, P., Davis, S. J., Fiore, A. M., Fletcher, S. M., Hertel, T. W., Horton, D. E., Hsiang, S.
703 M., Jackson, R. B., Jin, X., Levi, M., Lobell, D. B., McKinley, G. A., Moore, F. C., Montgomery,
704 A., Nadeau, K. C., Pataki, D. E., Randerson, J. T., Reichstein, M., Schnell, J. L., Seneviratne, S. I.,
705 Singh, D., Steiner, A. L., and Wong-Parodi, G.: The COVID-19 lockdowns: a window into the
706 Earth System, *Nat. Rev. Earth Environ.*, 1–12, <https://doi.org/10.1038/s43017-020-0079-1>, 2020.

707 Doumbia, T., Granier, C., Elguindi, N., Bouarar, I., Darras, S., Brasseur, G., Gaubert, B., Liu, Y.,
708 Shi, X., Stavrakou, T., Tilmes, S., Lacey, F., Deroubaix, A., and Wang, T.: Changes in global air
709 pollutant emissions during the COVID-19 pandemic: A dataset for atmospheric modeling, *Earth*

710 Syst. Sci. Data, 13, 4191–4206, <https://doi.org/10.5194/essd-13-4191-2021>, 2021.

711 Dutheil, F., Baker, J. S., and Navel, V.: COVID-19 as a factor influencing air pollution?, *Environ.*
712 *Pollut.*, 263, 2019–2021, <https://doi.org/10.1016/j.envpol.2020.114466>, 2020.

713 Emanuel, K. A.: A Scheme for Representing Cumulus Convection in Large-Scale Models, *J.*
714 *Atmos. Sci.*, 48, 2313–2329, [https://doi.org/10.1175/1520-
715 *0469\(1991\)048<2313:ASFRCC>2.0.CO;2*, 1991.](https://doi.org/10.1175/1520-0469(1991)048<2313:ASFRCC>2.0.CO;2)

716 Erisman, J. W., Bleeker, A., Galloway, J., and Sutton, M. S.: Reduced nitrogen in ecology and the
717 environment, *Environ. Pollut.*, 150, 140–149, <https://doi.org/10.1016/j.envpol.2007.06.033>, 2007.

718 Erisman, J. W., Sutton, M. a., Galloway, J., Klimont, Z., and Winiwarter, W.: How a century of
719 ammonia synthesis changed the world, *Nat. Geosci.*, 1, 636–639, <https://doi.org/10.1038/ngeo325>,
720 2008.

721 Evangeliou, N., Platt, S., Eckhardt, S., Lund Myhre, C., Laj, P., Alados-Arboledas, L., Backman, J.,
722 Brem, B., Fiebig, M., Flentje, H., Marinoni, A., Pandolfi, M., Yus-Diez, J., Prats, N., Putaud, J.,
723 Sellegri, K., Sorribas, M., Eleftheriadis, K., Vratolis, S., Wiedensohler, A., and Stohl, A.: Changes
724 in black carbon emissions over Europe due to COVID-19 lockdowns, *Atmos. Chem. Phys.*, 1–33,
725 <https://doi.org/10.5194/acp-2020-1005>, 2020.

726 Evangeliou, N., Balkanski, Y., Eckhardt, S., Cozic, A., Van Damme, M., Coheur, P.-F., Clarisse,
727 L., Shephard, M., Cady-Pereira, K., and Hauglustaine, D.: 10–Year Satellite–Constrained Fluxes of
728 Ammonia Improve Performance of Chemistry Transport Models, *Atmos. Chem. Phys.*, 21, 4431–
729 4451, <https://doi.org/10.5194/acp-21-4431-2021>, 2021.

730 Folberth, G. A., Hauglustaine, D. A., Lathièrre, J., and Brocheton, F.: Interactive chemistry in the
731 Laboratoire de Météorologie Dynamique general circulation model: model description and impact
732 analysis of biogenic hydrocarbons on tropospheric chemistry, *Atmos. Chem. Phys.*, 6, 2273–2319,
733 <https://doi.org/10.5194/acp-6-2273-2006>, 2006.

734 Forster, C., Stohl, A., and Seibert, P.: Parameterization of convective transport in a Lagrangian
735 particle dispersion model and its evaluation, *J. Appl. Meteorol. Climatol.*, 46, 403–422,
736 <https://doi.org/10.1175/JAM2470.1>, 2007.

737 Fowler, D., Muller, J. B. A., Smith, R. I., Dragosits, U., Skiba, U., Sutton, M. A., and
738 Brimblecombe, P.: A CHRONOLOGY OF NITROGEN DEPOSITION IN THE UK, *Water, Air,*
739 *Soil Pollut. Focus*, 4, 9–23, 2004.

740 Ge, X., Schaap, M., Kranenburg, R., Segers, A., Jan Reinds, G., Kros, H., and De Vries, W.:
741 Modeling atmospheric ammonia using agricultural emissions with improved spatial variability and
742 temporal dynamics, *Atmos. Chem. Phys.*, 20, 16055–16087, [https://doi.org/10.5194/acp-20-16055-](https://doi.org/10.5194/acp-20-16055-2020)
743 *2020*, 2020.

744 Giani, P., Castruccio, S., Anav, A., Howard, D., Hu, W., and Crippa, P.: Short-term and long-term

745 health impacts of air pollution reductions from COVID-19 lockdowns in China and Europe: a
746 modelling study, *Lancet Planet. Heal.*, 4, e474–e482, [https://doi.org/10.1016/S2542-](https://doi.org/10.1016/S2542-5196(20)30224-2)
747 [5196\(20\)30224-2](https://doi.org/10.1016/S2542-5196(20)30224-2), 2020.

748 Giglio, L., Randerson, J. T., and van der Werf, G. R.: Analysis of daily, monthly, and annual burned
749 area using the fourth-generation global fire emissions database (GFED4), *J. Geophys. Res.*
750 *Biogeosciences*, 118, 317–328, <https://doi.org/10.1002/jgrg.20042>, 2013, 2013.

751 Gordon, D. V., Grafton, R. Q., and Steinshamn, S. I.: Cross-country effects and policy responses to
752 COVID-19 in 2020: The Nordic countries, *Econ. Anal. Policy*, 71, 198–210,
753 <https://doi.org/10.1016/j.eap.2021.04.015>, 2021.

754 Gu, B., Sutton, M. A., Chang, S. X., Ge, Y., and Chang, J.: Agricultural ammonia emissions
755 contribute to China’s urban air pollution, *Front. Ecol. Environ.*, 12, 265–266,
756 <https://doi.org/10.1890/14.WB.007>, 2014.

757 Guevara, M., Jorba, O., Soret, A., Petetin, H., Bowdalo, D., Serradell, K., Tena, C., Van Der Gon,
758 H. D., Kuenen, J., Peuch, V. H., and Pérez García-Pando, C.: Time-resolved emission reductions for
759 atmospheric chemistry modelling in Europe during the COVID-19 lockdowns, *Atmos. Chem.*
760 *Phys.*, 21, 773–797, <https://doi.org/10.5194/acp-21-773-2021>, 2021.

761 Hauglustaine, D. A., Hourdin, F., Jourdain, L., Filiberti, M.-A., Walters, S., Lamarque, J.-F., and
762 Holland, E. A.: Interactive chemistry in the Laboratoire de Meteorologie Dynamique general
763 circulation model: Description and background tropospheric chemistry evaluation, *J. Geophys.*
764 *Res.*, 109, <https://doi.org/10.1029/2003JD003957>, 2004.

765 Hauglustaine, D. A., Balkanski, Y., and Schulz, M.: A global model simulation of present and
766 future nitrate aerosols and their direct radiative forcing of climate, *Atmos. Chem. Phys.*, 14, 11031–
767 11063, <https://doi.org/10.5194/acp-14-11031-2014>, 2014.

768 Heald, C. L., Collett, J. L., Lee, T., Benedict, K. B., Schwandner, F. M., Li, Y., Clarisse, L.,
769 Hurtmans, D. R., Van Damme, M., Clerbaux, C., Coheur, P. F., Philip, S., Martin, R. V., and Pye,
770 H. O. T.: Atmospheric ammonia and particulate inorganic nitrogen over the United States, *Atmos.*
771 *Chem. Phys.*, 12, 10295–10312, <https://doi.org/10.5194/acp-12-10295-2012>, 2012.

772 Henze, D. K., Shindell, D. T., Akhtar, F., Spurr, R. J. D., Pinder, R. W., Loughlin, D., Kopacz, M.,
773 Singh, K., and Shim, C.: Spatially Refined Aerosol Direct Radiative Forcing Efficiencies, *Environ.*
774 *Sci. Technol.*, 46, 9511–9518, <https://doi.org/10.1021/es301993s>, 2012.

775 Hersbach, H., Bell, B., Berrisford, P., Hirahara, S., Horányi, A., Muñoz-Sabater, J., Nicolas, J.,
776 Peubey, C., Radu, R., Schepers, D., Simmons, A., Soci, C., Abdalla, S., Abellan, X., Balsamo, G.,
777 Bechtold, P., Biavati, G., Bidlot, J., Bonavita, M., De Chiara, G., Dahlgren, P., Dee, D.,
778 Diamantakis, M., Dragani, R., Flemming, J., Forbes, R., Fuentes, M., Geer, A., Haimberger, L.,
779 Healy, S., Hogan, R. J., Hólm, E., Janisková, M., Keeley, S., Laloyaux, P., Lopez, P., Lupu, C.,

780 Radnoti, G., de Rosnay, P., Rozum, I., Vamborg, F., Villaume, S., and Thépaut, J. N.: The ERA5
781 global reanalysis, *Q. J. R. Meteorol. Soc.*, 146, 1999–2049, <https://doi.org/10.1002/qj.3803>, 2020.

782 Hourdin, F. and Armengaud, A.: The Use of Finite-Volume Methods for Atmospheric Advection of
783 Trace Species. Part I: Test of Various Formulations in a General Circulation Model, *Mon. Weather*
784 *Rev.*, 127, 822–837, [https://doi.org/10.1175/1520-0493\(1999\)127<0822:TUOFVM>2.0.CO;2](https://doi.org/10.1175/1520-0493(1999)127<0822:TUOFVM>2.0.CO;2),
785 1999.

786 Hourdin, F., Musat, I., Bony, S., Braconnot, P., Codron, F., Dufresne, J. L., Fairhead, L., Filiberti,
787 M. A., Friedlingstein, P., Grandpeix, J. Y., Krinner, G., LeVan, P., Li, Z. X., and Lott, F.: The
788 LMDZ4 general circulation model: Climate performance and sensitivity to parametrized physics
789 with emphasis on tropical convection, *Clim. Dyn.*, 27, 787–813, [https://doi.org/10.1007/s00382-](https://doi.org/10.1007/s00382-006-0158-0)
790 [006-0158-0](https://doi.org/10.1007/s00382-006-0158-0), 2006.

791 Hoyle, C. R., Fuchs, C., Jarvinen, E., Saathoff, H., Dias, A., El Haddad, I., Gysel, M., Coburn, S.
792 C., Trostl, J., Hansel, A., Bianchi, F., Breitenlechner, M., Corbin, J. C., Craven, J., Donahue, N. M.,
793 Duplissy, J., Ehrhart, S., Frege, C., Gordon, H., Hoppel, N., Heinritzi, M., Kristensen, T. B.,
794 Molteni, U., Nichman, L., Pinterich, T., Prevôt, A. S. H., Simon, M., Slowik, J. G., Steiner, G.,
795 Tome, A., Vogel, A. L., Volkamer, R., Wagner, A. C., Wagner, R., Wexler, A. S., Williamson, C.,
796 Winkler, P. M., Yan, C., Amorim, A., Dommen, J., Curtius, J., Gallagher, M. W., Flagan, R. C.,
797 Hansel, A., Kirkby, J., Kulmala, M., Mohler, O., Stratmann, F., Worsnop, D. R., and Baltensperger,
798 U.: Aqueous phase oxidation of sulphur dioxide by ozone in cloud droplets, *Atmos. Chem. Phys.*,
799 16, 1693–1712, <https://doi.org/10.5194/acp-16-1693-2016>, 2016.

800 Huang, X., Ding, A., Gao, J., Zheng, B., Zhou, D., Qi, X., Tang, R., Wang, J., Ren, C., Nie, W.,
801 Chi, X., Xu, Z., Chen, L., Li, Y., Che, F., Pang, N., Wang, H., Tong, D., Qin, W., Cheng, W., Liu,
802 W., Fu, Q., Liu, B., Chai, F., Davis, S. J., Zhang, Q., and He, K.: Enhanced secondary pollution
803 offset reduction of primary emissions during COVID-19 lockdown in China, *Natl. Sci. Rev.*, 8,
804 <https://doi.org/10.1093/nsr/nwaa137>, 2021.

805 Jackson, R. B., Friedlingstein, P., Quéré, C. Le, Abernethy, S., Andrew, R. M., Canadell, J. G.,
806 Ciais, P., Davis, S. J., Deng, Z., Liu, Z., Korsbakken, J. I., and Peters, G. P.: Global fossil carbon
807 emissions rebound near pre-COVID-19 levels, *Environ. Res. Lett.*, 17,
808 <https://doi.org/https://doi.org/10.1088/1748-9326/ac55b6>, 2022.

809 Kean, A. J., Littlejohn, D., Ban-Weiss, G. A., Harley, R. A., Kirchstetter, T. W., and Lunden, M.
810 M.: Trends in on-road vehicle emissions of ammonia, *Atmos. Environ.*, 43, 1565–1570,
811 <https://doi.org/10.1016/j.atmosenv.2008.09.085>, 2009.

812 Kharol, S. K., Shephard, M. W., McLinden, C. A., Zhang, L., Sioris, C. E., O'Brien, J. M., Vet, R.,
813 Cady-Pereira, K. E., Hare, E., Siemons, J., and Krotkov, N. A.: Dry Deposition of Reactive
814 Nitrogen From Satellite Observations of Ammonia and Nitrogen Dioxide Over North America,

815 Geophys. Res. Lett., 45, 1157–1166, <https://doi.org/10.1002/2017GL075832>, 2018.

816 Kirkby, J., Duplissy, J., Sengupta, K., Frege, C., Gordon, H., Williamson, C., Heinritzi, M., Simon,
817 M., Yan, C., Almeida, J., Trostl, J., Nieminen, T., Ortega, I. K., Wagner, R., Adamov, A., Amorim,
818 A., Bernhammer, A. K., Bianchi, F., Breitenlechner, M., Brilke, S., Chen, X., Craven, J., Dias, A.,
819 Ehrhart, S., Flagan, R. C., Franchin, A., Fuchs, C., Guida, R., Hakala, J., Hoyle, C. R., Jokinen, T.,
820 Junninen, H., Kangasluoma, J., Kim, J., Krapf, M., Kurten, A., Laaksonen, A., Lehtipalo, K.,
821 Makhmutov, V., Mathot, S., Molteni, U., Onnela, A., Perakyla, O., Piel, F., Petaja, T., Praplan, A.
822 P., Pringle, K., Rap, A., Richards, N. A. D., Riipinen, I., Rissanen, M. P., Rondo, L., Sarnela, N.,
823 Schobesberger, S., Scott, C. E., Seinfeld, J. H., Sipila, M., Steiner, G., Stozhkov, Y., Stratmann, F.,
824 Tomé, A., Virtanen, A., Vogel, A. L., Wagner, A. C., Wagner, P. E., Weingartner, E., Wimmer, D.,
825 Winkler, P. M., Ye, P., Zhang, X., Hansel, A., Dommen, J., Donahue, N. M., Worsnop, D. R.,
826 Baltensperger, U., Kulmala, M., Carslaw, K. S., and Curtius, J.: Ion-induced nucleation of pure
827 biogenic particles, *Nature*, 533, 521–526, <https://doi.org/10.1038/nature17953>, 2016.

828 Klimont, Z.: personal communication, 2022.

829 Klimont, Z., Kupiainen, K., Heyes, C., Purohit, P., Cofala, J., Rafaj, P., Borken-Kleefeld, J., and
830 Schöpp, W.: Global anthropogenic emissions of particulate matter including black carbon, *Atmos.*
831 *Chem. Phys.*, 17, 8681–8723, <https://doi.org/10.5194/acp-17-508681-2017>, 2017.

832 Krinner, G., Viovy, N., de Noblet-Ducoudré, N., Ogée, J., Polcher, J., Friedlingstein, P., Ciais, P.,
833 Sitch, S., and Prentice, I. C.: A dynamic global vegetation model for studies of the coupled
834 atmosphere-biosphere system, *Global Biogeochem. Cycles*, 19, GB1015,
835 <https://doi.org/10.1029/2003GB002199>, 2005.

836 Kristiansen, N. I., Stohl, A., Olivieri, D. J. L., Croft, B., Søvde, O. A., Klein, H., Christoudias, T.,
837 Kunkel, D., Leadbetter, S. J., Lee, Y. H., Zhang, K., Tsigaridis, K., Bergman, T., Evangeliou, N.,
838 Wang, H., Ma, P. L., Easter, R. C., Rasch, P. J., Liu, X., Pitari, G., Di Genova, G., Zhao, S. Y.,
839 Balkanski, Y., Bauer, S. E., Faluvegi, G. S., Kokkola, H., Martin, R. V., Pierce, J. R., Schulz, M.,
840 Shindell, D., Tost, H., and Zhang, H.: Evaluation of observed and modelled aerosol lifetimes using
841 radioactive tracers of opportunity and an ensemble of 19 global models, 3525–3561 pp.,
842 <https://doi.org/10.5194/acp-16-3525-2016>, 2016.

843 Krupa, S. V.: Effects of atmospheric ammonia (NH₃) on terrestrial vegetation: A review, *Environ.*
844 *Pollut.*, 124, 179–221, [https://doi.org/10.1016/S0269-7491\(02\)00434-7](https://doi.org/10.1016/S0269-7491(02)00434-7), 2003.

845 Kuttippurath, J., Patel, V. K., Kashyap, R., Singh, A., and Clerbaux, C.: Anomalous increase in
846 global atmospheric ammonia during COVID-19 lockdown: Need for policies to curb agricultural
847 emissions, *J. Clean. Prod.*, 434, 140424, <https://doi.org/10.1016/j.jclepro.2023.140424>, 2023.

848 Lachatre, M., Fortems-Cheiney, A., Foret, G., Siour, G., Dufour, G., Clarisse, L., Clerbaux, C.,
849 Coheur, P. F., Van Damme, M., and Beekmann, M.: The unintended consequence of SO₂ and NO₂

850 regulations over China: Increase of ammonia levels and impact on PM_{2.5} concentrations, *Atmos.*
851 *Chem. Phys.*, 19, 6701–6716, <https://doi.org/10.5194/acp-19-6701-2019>, 2019.

852 Le, T., Wang, Y., Liu, L., Yang, J., Yung, Y. L., Li, G., and Seinfeld, J. H.: Unexpected air
853 pollution with marked emission reductions during the COVID-19 outbreak in China, *Science* (80-
854), eabb7431, <https://doi.org/10.1126/science.abb7431>, 2020.

855 Lelieveld, J., Evans, J. S., Fnais, M., Giannadaki, D., and Pozzer, A.: The contribution of outdoor
856 air pollution sources to premature mortality on a global scale., *Nature*, 525, 367–71,
857 <https://doi.org/10.1038/nature15371>, 2015.

858 Leung, D. M., Shi, H., Zhao, B., Wang, J., Ding, E. M., Gu, Y., Zheng, H., Chen, G., Liou, K. N.,
859 Wang, S., Fast, J. D., Zheng, G., Jiang, J., Li, X., and Jiang, J. H.: Wintertime Particulate Matter
860 Decrease Buffered by Unfavorable Chemical Processes Despite Emissions Reductions in China,
861 *Geophys. Res. Lett.*, 47, 1–12, <https://doi.org/10.1029/2020GL087721>, 2020.

862 Li, B., Ma, Y., Zhou, Y., and Chai, E.: Research progress of different components of PM_{2.5} and
863 ischemic stroke, *Sci. Rep.*, 13, 1–12, <https://doi.org/10.1038/s41598-023-43119-5>, 2023.

864 Li, C., Martin, R. V., Shephard, M. W., Pereira, K. C., Cooper, M. J., Kaiser, J., Lee, C. J., Zhang,
865 L., and Henze, D. K.: Assessing the Iterative Finite Difference Mass Balance and 4D - Var Methods
866 to Derive Ammonia Emissions Over North America Using Synthetic Observations, *J. Geophys.*
867 *Res. Atmos.*, 124, 4222–4236, <https://doi.org/10.1029/2018JD030183>, 2019.

868 Li, L., Li, Q., Huang, L., Wang, Q., Zhu, A., Xu, J., Liu, Z., Li, H., Shi, L., Li, R., Azari, M., Wang,
869 Y., Zhang, X., Liu, Z., Zhu, Y., Zhang, K., Xue, S., Ooi, M. C. G., Zhang, D., and Chan, A.: Air
870 quality changes during the COVID-19 lockdown over the Yangtze River Delta Region: An insight
871 into the impact of human activity pattern changes on air pollution variation, *Sci. Total Environ.*,
872 732, <https://doi.org/10.1016/j.scitotenv.2020.139282>, 2020.

873 Liu, L., Li, H., Zhang, H., Zhong, J., Bai, Y., Ge, M., Li, Z., Chen, Y., and Zhang, X.: The role of
874 nitric acid in atmospheric new particle formation, *Phys. Chem. Chem. Phys.*, 20, 17406–17414,
875 <https://doi.org/10.1039/C8CP02719F>, 2018.

876 Lovarelli, D., Fugazza, D., Costantini, M., Conti, C., Diolaiuti, G., and Guarino, M.: Comparison of
877 ammonia air concentration before and during the spread of COVID-19 in Lombardy (Italy) using
878 ground-based and satellite data, *Atmos. Environ.*, 259, 118534,
879 <https://doi.org/10.1016/j.atmosenv.2021.118534>, 2021.

880 Malm, W. C.: Spatial and monthly trends in speciated fine particle concentration in the United
881 States, *J. Geophys. Res.*, 109, D03306, <https://doi.org/10.1029/2003JD003739>, 2004.

882 Matthias, V., Quante, M., Arndt, J. A., Badeke, R., Fink, L., Petrik, R., Feldner, J., Schwarzkopf,
883 D., Link, E. M., Ramacher, M. O. P., and Wedemann, R.: The role of emission reductions and the
884 meteorological situation for air quality improvements during the COVID-19 lockdown period in

885 central Europe, *Atmos. Chem. Phys.*, 21, 13931–13971, <https://doi.org/10.5194/acp-21-13931->
886 2021, 2021.

887 Mo, Z., Huang, J., Chen, Z., Zhou, B., Zhu, K., Liu, H., Mu, Y., Zhang, D., and Wang, S.: Cause
888 analysis of PM_{2.5} pollution during the COVID-19 lockdown in Nanning, China, *Sci. Rep.*, 11, 1–
889 13, <https://doi.org/10.1038/s41598-021-90617-5>, 2021.

890 Pai, S. J., Heald, C. L., and Murphy, J. G.: Exploring the Global Importance of Atmospheric
891 Ammonia Oxidation, *ACS Earth Sp. Chem.*, 5, 1674–1685,
892 <https://doi.org/10.1021/acsearthspacechem.1c00021>, 2021.

893 Patel, H., Talbot, N., Salmond, J., Dirks, K., Xie, S., and Davy, P.: Implications for air quality
894 management of changes in air quality during lockdown in Auckland (New Zealand) in response to
895 the 2020 SARS-CoV-2 epidemic, *Sci. Total Environ.*, 746, 141129,
896 <https://doi.org/10.1016/j.scitotenv.2020.141129>, 2020.

897 Paulot, F., Jacob, D. J., Pinder, R. W., Bash, J. O., Travis, K., and Henze, D. K.: Ammonia
898 emissions in the United States, European Union, and China derived by high-resolution inversion of
899 ammonium wet deposition data: Interpretation with a new agricultural emissions inventory
900 (MASAGE-NH₃), *J. Geophys. Res. Atmos.*, 119, 4343–4364,
901 <https://doi.org/10.1002/2013JD021130>, 2014.

902 Pisso, I., Sollum, E., Grythe, H., Kristiansen, N., Cassiani, M., Eckhardt, S., Arnold, D., Morton,
903 D., Thompson, R. L., Groot Zwaafink, C. D., Evangeliou, N., Sodemann, H., Haimberger, L.,
904 Henne, S., Brunner, D., Burkhardt, J. F., Fouilloux, A., Brioude, J., Philipp, A., Seibert, P., and
905 Stohl, A.: The Lagrangian particle dispersion model FLEXPART version 10.4, *Geosci. Model Dev.*,
906 12, 4955–4997, <https://doi.org/10.5194/gmd-12-4955-2019>, 2019.

907 Pope, C. A. and Dockery, D. W.: Health effects of fine particulate air pollution: Lines that connect,
908 *J. Air Waste Manag. Assoc.*, 56, 709–742, <https://doi.org/10.1080/10473289.2006.10464485>, 2006.

909 Pope III, C. A., Burnett, R. T., Thun, M. J., Calle, E. E., Krewski, D., and Thurston, G. D.: Lung
910 Cancer, Cardiopulmonary Mortality, and Long-term Exposure to Fine Particulate Air Pollution, *J.*
911 *Am. Med. Assoc.*, 287, 1132–1141, <https://doi.org/10.1001/jama.287.9.1132>, 2002.

912 Pozzer, A., Tsimpidi, A. P., Karydis, V. A., De Meij, A., and Lelieveld, J.: Impact of agricultural
913 emission reductions on fine-particulate matter and public health, *Atmos. Chem. Phys.*, 17, 12813–
914 12826, <https://doi.org/10.5194/acp-17-12813-2017>, 2017.

915 Putaud, J. P., Pozzoli, L., Pisoni, E., Martins Dos Santos, S., Lagler, F., Lanzani, G., Dal Santo, U.,
916 and Colette, A.: Impacts of the COVID-19 lockdown on air pollution at regional and urban
917 background sites in northern Italy, *Atmos. Chem. Phys.*, 21, 7597–7609,
918 <https://doi.org/10.5194/acp-21-7597-2021>, 2021.

919 Putaud, J. P., Pisoni, E., Mangold, A., Hueglin, C., Sciare, J., Pikridas, M., Savvides, C., Ondracek,

920 J., Mbengue, S., Wiedensohler, A., Weinhold, K., Merkel, M., Poulain, L., Van Pinxteren, D.,
921 Herrmann, H., Massling, A., Nordstroem, C., Alastuey, A., Reche, C., Pérez, N., Castillo, S.,
922 Sorribas, M., Adame, J. A., Petaja, T., Lehtipalo, K., Niemi, J., Riffault, V., De Brito, J. F., Colette,
923 A., Favez, O., Petit, J. E., Gros, V., Gini, M. I., Vratolis, S., Eleftheriadis, K., Diapouli, E., Denier
924 Van Der Gon, H., Yttri, K. E., and Aas, W.: Impact of 2020 COVID-19 lockdowns on particulate
925 air pollution across Europe, *Atmos. Chem. Phys.*, 23, 10145–10161, [https://doi.org/10.5194/acp-23-](https://doi.org/10.5194/acp-23-10145-2023)
926 10145-2023, 2023.

927 Querol, X., Massagué, J., Alastuey, A., Moreno, T., Gangoiti, G., Mantilla, E., Duéguéz, J. J.,
928 Escudero, M., Monfort, E., Pérez García-Pando, C., Petetin, H., Jorba, O., Vázquez, V., de la Rosa,
929 J., Campos, A., Muñoz, M., Monge, S., Hervás, M., Javato, R., and Cornide, M. J.: Lessons from
930 the COVID-19 air pollution decrease in Spain: Now what?, *Sci. Total Environ.*, 779,
931 <https://doi.org/10.1016/j.scitotenv.2021.146380>, 2021.

932 Reche, C., Viana, M., Pandolfi, M., Alastuey, A., Moreno, T., Amato, F., Ripoll, A., and Querol,
933 X.: Urban NH₃ levels and sources in a Mediterranean environment, *Atmos. Environ.*, 57, 153–164,
934 <https://doi.org/10.1016/j.atmosenv.2012.04.021>, 2012.

935 Rennie, S., Watkins, J., Ball, L., Brown, M., Fry, M., Henrys, P., Hollaway, M., Quinn, J., Sier, A.,
936 and Dick, J.: Shaping the development of the UKCEH UK-SCAPE Data Science Framework.
937 Workshop report, 2020.

938 Rodgers, C. D.: *Inverse Methods for Atmospheric Sounding*, WORLD SCIENTIFIC, 256 pp.,
939 <https://doi.org/doi:10.1142/3171>, 2000.

940 Schobesberger, S., Franchin, A., Bianchi, F., Rondo, L., Duplissy, J., Kürten, A., Ortega, I. K.,
941 Metzger, A., Schnitzhofer, R., Almeida, J., Amorim, A., Dommen, J., Dunne, E. M., Ehn, M.,
942 Gagné, S., Ickes, L., Junninen, H., Hansel, A., Kerminen, V. M., Kirkby, J., Kupc, A., Laaksonen,
943 A., Lehtipalo, K., Mathot, S., Onnela, A., Petäjä, T., Riccobono, F., Santos, F. D., Sipilä, M., Tomé,
944 A., Tsagkogeorgas, G., Viisanen, Y., Wagner, P. E., Wimmer, D., Curtius, J., Donahue, N. M.,
945 Baltensperger, U., Kulmala, M., and Worsnop, D. R.: On the composition of ammonia-sulfuric-acid
946 ion clusters during aerosol particle formation, *Atmos. Chem. Phys.*, 15, 55–78,
947 <https://doi.org/10.5194/acp-15-55-2015>, 2015.

948 Seinfeld, J. H. and Pandis, S. N.: *Atmospheric Chemistry and Physics. From Air Pollution to*
949 *Climate Change*, 2nd ed., John Wiley & Sons, NY, 2000.

950 Shephard, M. W. and Cady-Pereira, K. E.: Cross-track Infrared Sounder (CrIS) satellite
951 observations of tropospheric ammonia, *Atmos. Meas. Tech.*, 8, 1323–1336,
952 <https://doi.org/10.5194/amt-8-1323-2015>, 2015.

953 Shephard, M. W., McLinden, C. A., Cady-Pereira, K. E., Luo, M., Moussa, S. G., Leithead, A.,
954 Liggio, J., Staebler, R. M., Akingunola, A., Makar, P., Lehr, P., Zhang, J., Henze, D. K., Millet, D.

955 B., Bash, J. O., Zhu, L., Wells, K. C., Capps, S. L., Chaliyakunnel, S., Gordon, M., Hayden, K.,
956 Brook, J. R., Wolde, M., and Li, S. M.: Tropospheric Emission Spectrometer (TES) satellite
957 observations of ammonia, methanol, formic acid, and carbon monoxide over the Canadian oil sands:
958 Validation and model evaluation, *Atmos. Meas. Tech.*, 8, 5189–5211, [https://doi.org/10.5194/amt-](https://doi.org/10.5194/amt-8-5189-2015)
959 [8-5189-2015](https://doi.org/10.5194/amt-8-5189-2015), 2015.

960 Shephard, M. W., Dammers, E., E. Cady-Pereira, K., K. Kharol, S., Thompson, J., Gainariu-Matz,
961 Y., Zhang, J., A. McLinden, C., Kovachik, A., Moran, M., Bittman, S., E. Sioris, C., Griffin, D., J.
962 Alvarado, M., Lonsdale, C., Savic-Jovicic, V., and Zheng, Q.: Ammonia measurements from space
963 with the Cross-track Infrared Sounder: Characteristics and applications, *Atmos. Chem. Phys.*, 20,
964 2277–2302, <https://doi.org/10.5194/acp-20-2277-2020>, 2020.

965 Shi, X. and Brasseur, G. P.: The Response in Air Quality to the Reduction of Chinese Economic
966 Activities During the COVID-19 Outbreak, *Geophys. Res. Lett.*, 47, 1–8,
967 <https://doi.org/10.1029/2020GL088070>, 2020.

968 Shi, Z., Song, C., Liu, B., Lu, G., Xu, J., Van Vu, T., Elliott, R. J. R., Li, W., Bloss, W. J., and
969 Harrison, R. M.: Abrupt but smaller than expected changes in surface air quality attributable to
970 COVID-19 lockdowns, *Sci. Adv.*, 7, <https://doi.org/10.1126/sciadv.abd6696>, 2021.

971 Sicard, P., De Marco, A., Agathokleous, E., Feng, Z., Xu, X., Paoletti, E., Rodriguez, J. J. D., and
972 Calatayud, V.: Amplified ozone pollution in cities during the COVID-19 lockdown, *Sci. Total*
973 *Environ.*, 735, <https://doi.org/10.1016/j.scitotenv.2020.139542>, 2020.

974 Sitwell, M., Shephard, M., Rochon, Y., Cady-Pereira, K., and Dammers, E.: An Ensemble-
975 Variational Inversion System for the Estimation of Ammonia Emissions using CrIS Satellite
976 Ammonia Retrievals, 22, 6595–6624, <https://doi.org/10.5194/acp-22-6595-2022>, 2022.

977 Sohrabi, C., Alsafi, Z., O’Neill, N., Khan, M., Kerwan, A., Al-Jabir, A., Iosifidis, C., and Agha, R.:
978 World Health Organization declares global emergency: A review of the 2019 novel coronavirus
979 (COVID-19), *Int. J. Surg.*, 76, 71–76, <https://doi.org/10.1016/j.ijisu.2020.02.034>, 2020.

980 Sørensen, L. L., Hertel, O., Skjøth, C. A., Lund, M., and Pedersen, B.: Fluxes of ammonia in the
981 coastal marine boundary layer, *Atmos. Environ.*, 37, 167–177, [https://doi.org/10.1016/S1352-](https://doi.org/10.1016/S1352-2310(03)00247-4)
982 [2310\(03\)00247-4](https://doi.org/10.1016/S1352-2310(03)00247-4), 2003.

983 Stevens, C. J., Dupr, C., Dorland, E., Gaudnik, C., Gowing, D. J. G., Bleeker, A., Diekmann, M.,
984 Alard, D., Bobbink, R., Fowler, D., Corcket, E., Mountford, J. O., Vandvik, V., Aarrestad, P. A.,
985 Muller, S., and Dise, N. B.: Nitrogen deposition threatens species richness of grasslands across
986 Europe, *Environ. Pollut.*, 158, 2940–2945, <https://doi.org/10.1016/j.envpol.2010.06.006>, 2010.

987 Stohl, A., Forster, C., Frank, A., Seibert, P., and Wotawa, G.: Technical note: The Lagrangian
988 particle dispersion model FLEXPART version 6.2, *Atmos. Chem. Phys.*, 5, 2461–2474,
989 <https://doi.org/10.5194/acp-5-2461-2005>, 2005.

990 Sutton, M. A., Dragosits, U., Tang, Y. S., and Fowler, D.: Ammonia emissions from non-
991 agricultural sources in the UK, 34, 2000a.

992 Sutton, M. A., Dragosits, U., Tang, Y. S., and Fowler, D.: Ammonia emissions from non-
993 agricultural sources in the UK, *Atmos. Environ.*, 34, 855–869, 2000b.

994 Sutton, M. A., Erisman, J. W., Dentener, F., and Möller, D.: Ammonia in the environment: From
995 ancient times to the present, *Environ. Pollut.*, 156, 583–604,
996 <https://doi.org/10.1016/j.envpol.2008.03.013>, 2008.

997 Sutton, M. A., Reis, S., Riddick, S. N., Dragosits, U., Nemitz, E., Theobald, M. R., Tang, Y. S.,
998 Braban, C. F., Vieno, M., Dore, A. J., Mitchell, R. F., Wanless, S., Daunt, F., Fowler, D., Blackall,
999 T. D., Milford, C., Flechard, C. R., Loubet, B., Massad, R., Cellier, P., Personne, E., Coheur, P. F.,
1000 Clarisse, L., Damme, M. Van, Ngadi, Y., Clerbaux, C., Skjøth, C. A., Geels, C., Hertel, O., Kruit,
1001 R. J. W., Pinder, R. W., Bash, J. O., Walker, J. T., Simpson, D., Horvath, L., Misselbrook, T. H.,
1002 Bleeker, A., Dentener, F., and Vries, W. de: Towards a climate-dependent paradigm of ammonia
1003 emission and deposition, *Philos. Trans. R. Soc. B Biol. Sci.*, 368, 20130166–20130166,
1004 <https://doi.org/10.1098/rstb.2013.0166>, 2013.

1005 Szczepańska, A. and Pietrzyka, K.: The COVID-19 epidemic in Poland and its influence on the
1006 quality of life of university students (young adults) in the context of restricted access to public
1007 spaces, *J. Public Heal.*, <https://doi.org/10.1007/s10389-020-01456-z>, 2021.

1008 Thunis, P., Clappier, A., Beekmann, M., Putaud, J. P., Cuvelier, C., Madrazo, J., and De Meij, A.:
1009 Non-linear response of PM_{2.5} to changes in NO_x and NH₃ emissions in the Po basin (Italy):
1010 Consequences for air quality plans, *Atmos. Chem. Phys.*, 21, 9309–9327,
1011 <https://doi.org/10.5194/acp-21-9309-2021>, 2021.

1012 Tichý, O., Šmídl, V., Hofman, R., and Stohl, A.: LS-APC v1.0: A tuning-free method for the linear
1013 inverse problem and its application to source-Term determination, *Geosci. Model Dev.*, 9, 4297–
1014 4311, <https://doi.org/10.5194/gmd-9-4297-2016>, 2016.

1015 Tichý, O., Ulrych, L., Šmídl, V., Evangelidou, N., and Stohl, A.: On the tuning of atmospheric
1016 inverse methods: Comparisons with the European Tracer Experiment (ETEX) and Chernobyl
1017 datasets using the atmospheric transport model FLEXPART, *Geosci. Model Dev.*, 13, 5917–5934,
1018 <https://doi.org/10.5194/gmd-13-5917-2020>, 2020.

1019 Tichý, O., Eckhardt, S., Balkanski, Y., Hauglustaine, D., and Evangelidou, N.: Decreasing trends of
1020 ammonia emissions over Europe seen from remote sensing and inverse modelling, *Atmos. Chem.*
1021 *Phys.*, 23, 15235–15252, <https://doi.org/10.5194/acp-23-15235-2023>, 2023.

1022 Varotsos, C., Christodoulakis, J., Kouremadas, G. A., and Fotaki, E. F.: The Signature of the
1023 Coronavirus Lockdown in Air Pollution in Greece, *Water. Air. Soil Pollut.*, 232,
1024 <https://doi.org/10.1007/s11270-021-05055-w>, 2021.

1025 Viatte, C., Petit, J. E., Yamanouchi, S., Van Damme, M., Doucerain, C., Germain-Piaulenne, E.,
1026 Gros, V., Favez, O., Clarisse, L., Coheur, P. F., Strong, K., and Clerbaux, C.: Ammonia and pm2.5
1027 air pollution in paris during the 2020 covid lockdown, *Atmosphere (Basel)*, 12, 1–18,
1028 <https://doi.org/10.3390/atmos12020160>, 2021.

1029 De Vries, W., Kros, J., Reinds, G. J., and Butterbach-Bahl, K.: Quantifying impacts of nitrogen use
1030 in European agriculture on global warming potential, *Curr. Opin. Environ. Sustain.*, 3, 291–302,
1031 <https://doi.org/10.1016/j.cosust.2011.08.009>, 2011.

1032 Walters, W. W., Chai, J., and Hastings, M. G.: Theoretical Phase Resolved Ammonia-Ammonium
1033 Nitrogen Equilibrium Isotope Exchange Fractionations: Applications for Tracking Atmospheric
1034 Ammonia Gas-to-Particle Conversion, *ACS Earth Sp. Chem.*, 3, 79–89,
1035 <https://doi.org/10.1021/acsearthspacechem.8b00140>, 2019.

1036 Wang, M., Xiao, M., Bertozzi, B., Marie, G., Rörup, B., Schulze, B., Bardakov, R., He, X. C., Shen,
1037 J., Scholz, W., Marten, R., Dada, L., Baalbaki, R., Lopez, B., Lamkaddam, H., Manninen, H. E.,
1038 Amorim, A., Ataei, F., Bogert, P., Brasseur, Z., Caudillo, L., De Menezes, L. P., Duplissy, J.,
1039 Ekman, A. M. L., Finkenzeller, H., Carracedo, L. G., Granzin, M., Guida, R., Heinritzi, M.,
1040 Hofbauer, V., Höhler, K., Korhonen, K., Krechmer, J. E., Kürten, A., Lehtipalo, K., Mahfouz, N. G.
1041 A., Makhmutov, V., Massabò, D., Mathot, S., Mauldin, R. L., Mentler, B., Müller, T., Onnela, A.,
1042 Petäjä, T., Philippov, M., Piedehierro, A. A., Pozzer, A., Ranjithkumar, A., Schervish, M.,
1043 Schobesberger, S., Simon, M., Stozhkov, Y., Tomé, A., Umo, N. S., Vogel, F., Wagner, R., Wang,
1044 D. S., Weber, S. K., Welti, A., Wu, Y., Zauner-Wieczorek, M., Sipilä, M., Winkler, P. M., Hansel,
1045 A., Baltensperger, U., Kulmala, M., Flagan, R. C., Curtius, J., Riipinen, I., Gordon, H., Lelieveld,
1046 J., El-Haddad, I., Volkamer, R., Worsnop, D. R., Christoudias, T., Kirkby, J., Möhler, O., and
1047 Donahue, N. M.: Synergistic HNO₃–H₂SO₄–NH₃ upper tropospheric particle formation, *Nature*,
1048 605, 483–489, <https://doi.org/10.1038/s41586-022-04605-4>, 2022.

1049 Wang, P., Chen, K., Zhu, S., Wang, P., and Zhang, H.: Severe air pollution events not avoided by
1050 reduced anthropogenic activities during COVID-19 outbreak, *Resour. Conserv. Recycl.*, 158,
1051 104814, <https://doi.org/10.1016/j.resconrec.2020.104814>, 2020.

1052 Weber, R. J., McMurry, P. H., Mauldin, R. L., Tanner, D. J., Eisele, F. L., Clarke, A. D., and
1053 Kapustin, V. N.: New particle formation in the remote troposphere: A comparison of observations
1054 at various sites, *Geophys. Res. Lett.*, 26, 307–310, <https://doi.org/10.1029/1998GL900308>, 1999.

1055 White, E., Shephard, M. W., Cady-Pereira, K. E., Kharol, S. K., Ford, S., Dammers, E., Chow, E.,
1056 Thiessen, N., Tobin, D., Quinn, G., O’Brien, J., and Bash, J.: Accounting for Non-Detects:
1057 Application to Satellite Ammonia Observations, *Remote Sens.*, 15,
1058 <https://doi.org/10.3390/rs15102610>, 2023.

1059 Xu, W., Zhao, Y., Wen, Z., Chang, Y., Pan, Y., Sun, Y., and Ma, X.: Increasing importance of

1060 ammonia emission abatement in PM_{2.5} pollution control, *Sci. Bull.*, 67, 1745–1749,
1061 <https://doi.org/10.1016/j.scib.2022.07.021>, 2022.

1062 Zavyalov, V., Esplin, M., Scott, D., Esplin, B., Bingham, G., Hoffman, E., Lietzke, C., Predina, J.,
1063 Frain, R., Suwinski, L., Han, Y., Major, C., Graham, B., and Phillips, L.: Noise performance of the
1064 CrIS instrument, *J. Geophys. Res. Atmos.*, 118, 108–120, <https://doi.org/10.1002/2013JD020457>,
1065 2013.

1066 Zhai, S., Jacob, D. J., Wang, X., Liu, Z., Wen, T., Shah, V., Li, K., Moch, J. M., Bates, K. H., Song,
1067 S., Shen, L., Zhang, Y., Luo, G., Yu, F., Sun, Y., Wang, L., Qi, M., Tao, J., Gui, K., Xu, H., Zhang,
1068 Q., Zhao, T., Wang, Y., Lee, H. C., Choi, H., and Liao, H.: Control of particulate nitrate air
1069 pollution in China, *Nat. Geosci.*, 14, 389–395, <https://doi.org/10.1038/s41561-021-00726-z>, 2021.

1070 Zhang, X., Zhang, Z., Xiao, Z., Tang, G., Li, H., Gao, R., Dao, X., Wang, Y., and Wang, W.: Heavy
1071 haze pollution during the COVID-19 lockdown in the Beijing-Tianjin-Hebei region, China, *J.*
1072 *Environ. Sci. (China)*, 114, 170–178, <https://doi.org/10.1016/j.jes.2021.08.030>, 2022.

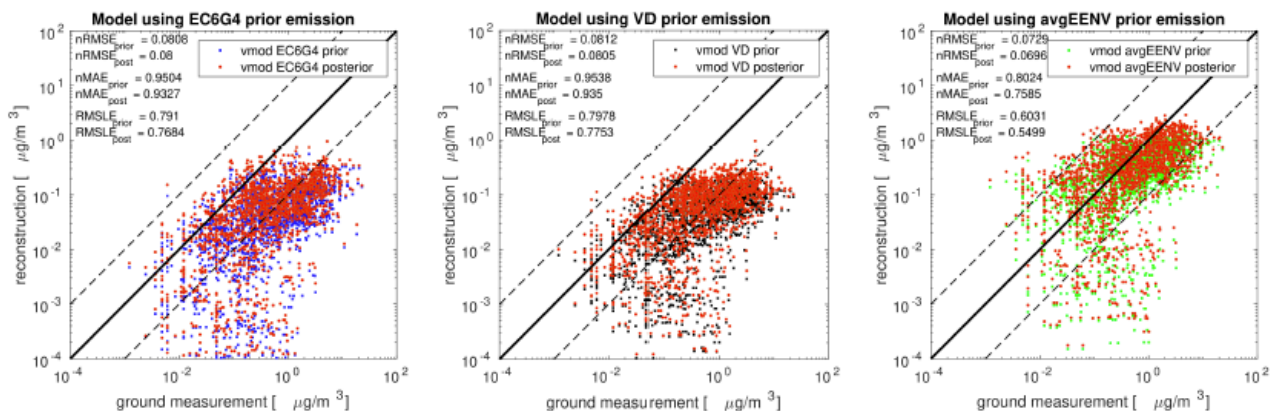
1073 Zhang, Y., Zhang, C., Liu, Z., and Yang, X.: Air pollution reduction during COVID-19 lockdown
1074 in China: a sustainable impact assessment for future cities development, *City Built Environ.*, 1, 1–
1075 21, <https://doi.org/10.1007/s44213-023-00013-0>, 2023.

1076

1077

1078 **FIGURE LEGENDS**

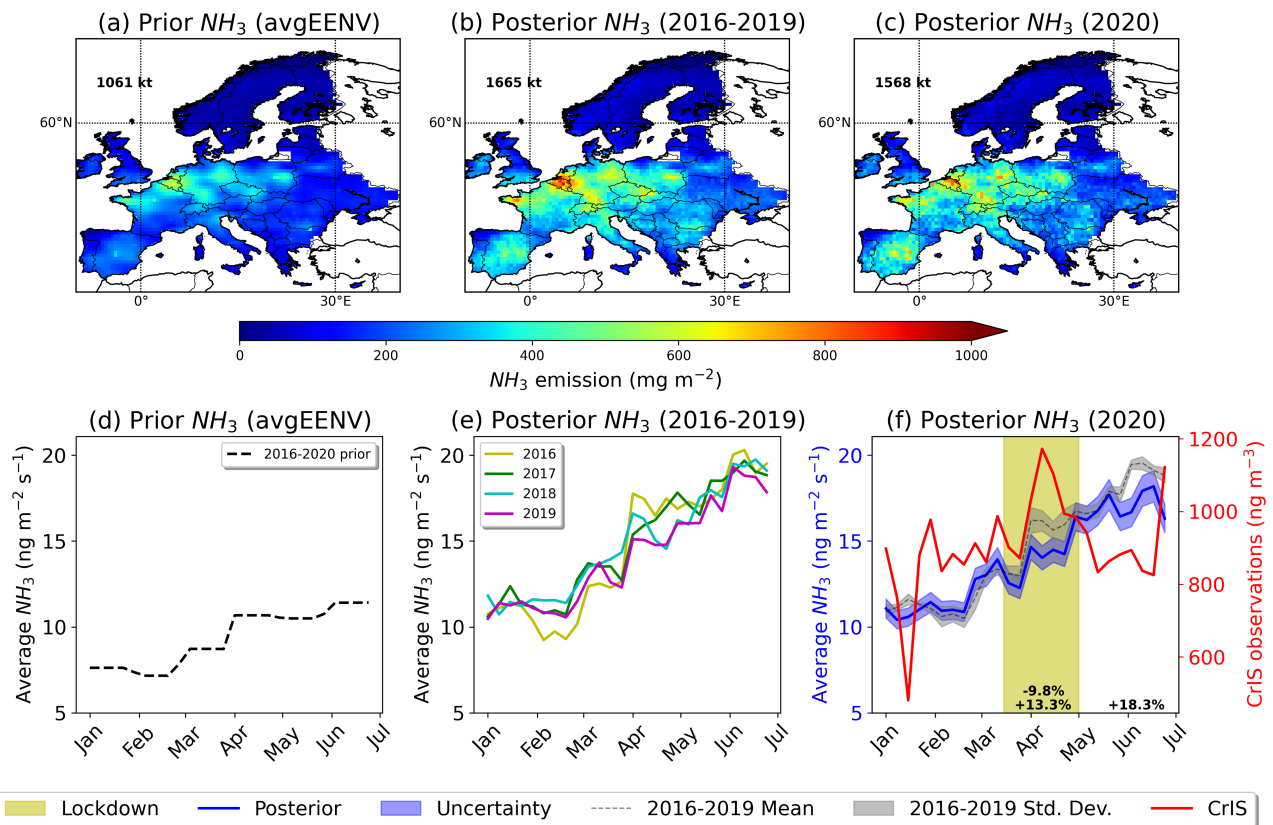
1079



1080

1081 **Figure 1.** Scatter plots of prior and posterior concentrations against independent observations
 1082 (observations that were not included in the inversion algorithm) from the EMEP network
 1083 (<https://emep.int/mscw/>, **Figure S 1**) from January to July 2020. Three statistical measures
 1084 (nRMSE, nMAE and RMSLE) were used to assess the performance of each inversion using three
 1085 different prior emission inventories for ammonia (EC6G4, VD and avgEENV).

1086

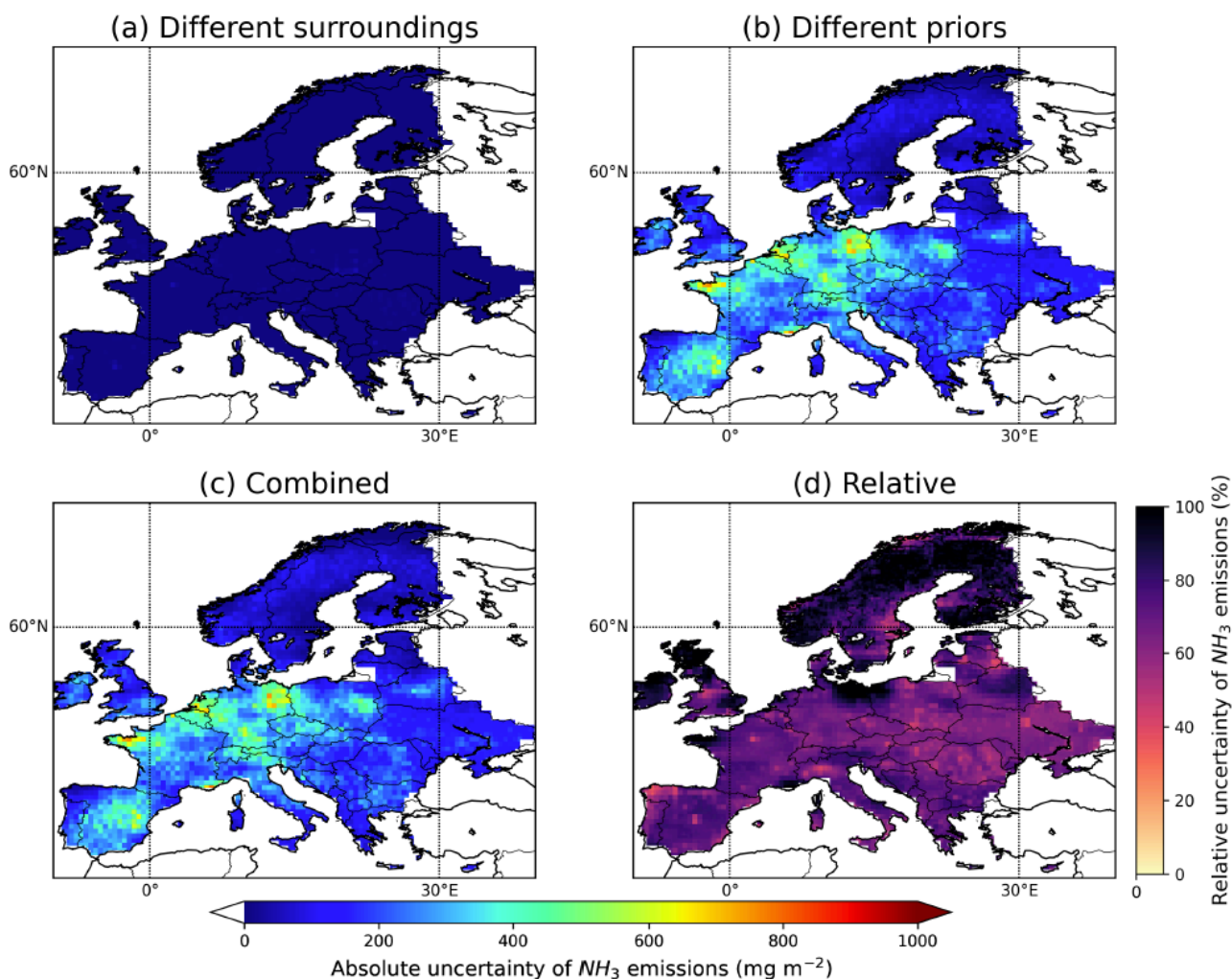


1087

1088 **Figure 2.** (a) Total a priori emissions of ammonia over Europe for the inversion period (January –
 1089 June). The emissions correspond to avgEENV prior, and the total emitted amount is equal to 1061 kt.
 1090 (b) Total a posteriori emissions of ammonia over Europe for the inversion period (January – June)
 1091 for the reference period 2016 – 2019 (using avgEENV prior) that amount 1665 kt. (c) Total posterior
 1092 emissions of ammonia over Europe for January – June 2020 (1568 kt) using the avgEENV as the
 1093 prior. (d) Timeseries of weekly-average prior emissions of ammonia over Europe (January to June
 1094 2020) from avgEENV prior. (e) Timeseries of weekly-average posterior emissions of ammonia over
 1095 Europe for the reference years 2016–2019 (January to June) (yellow, green, cyan, magenta colors).
 1096 (f) Timeseries of weekly-average posterior emissions of ammonia with the associated uncertainties
 1097 over Europe in 2020 resulting from inversions using the avgEENV prior are plotted together with the
 1098 CrIS observations averaged over Europe (red line) and the mean ammonia emissions with the
 1099 calculated standard deviations for the reference period (2016–2019). The single top number -9.8%
 1100 shows percentage change in ammonia emissions during the 2020 lockdown as compared to the same
 1101 period in reference years, whereas two bottom ones show the corresponding changes in ammonia
 1102 emissions (i) during the 2020 lockdown as compared to the period before lockdown (+13.3%), and
 1103 (ii) the period after lockdown finished as compared to the lockdown period +18.3%), known as
 1104 rebound period.

1105

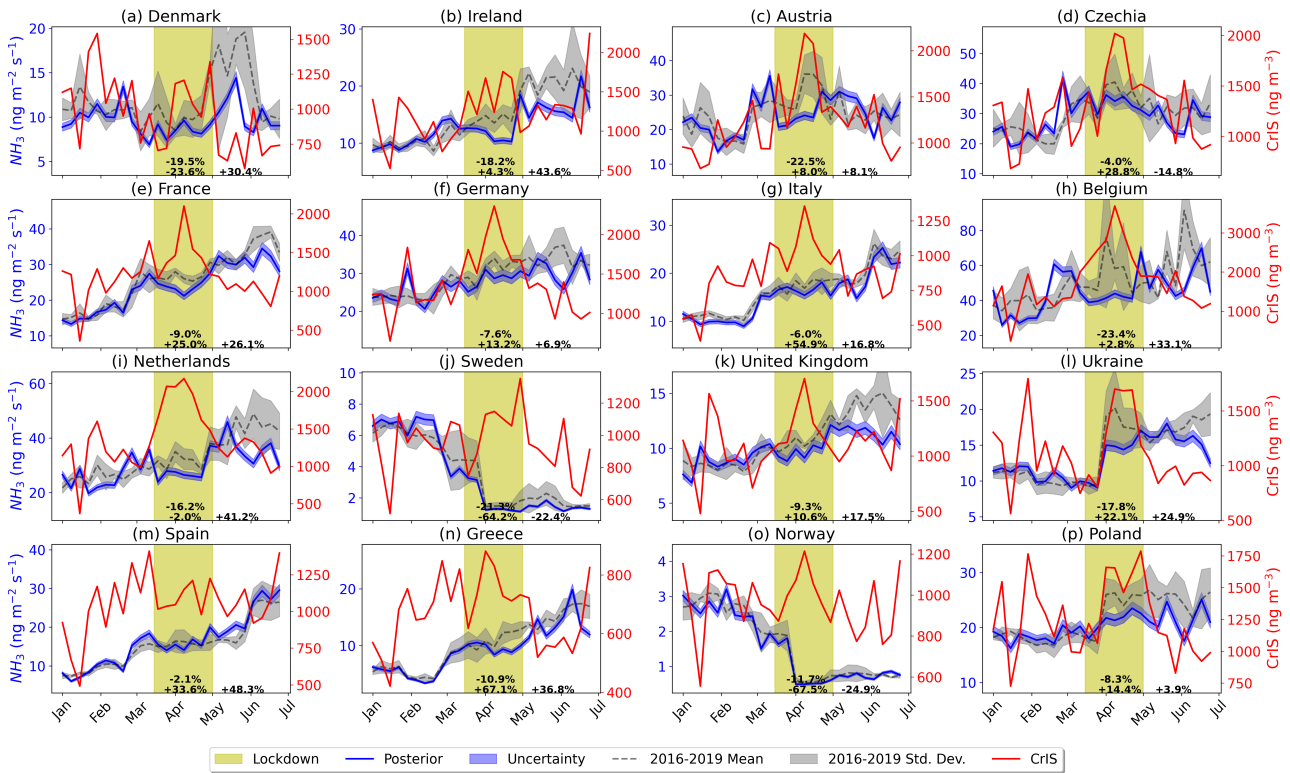
1106



1108

1109 **Figure 3.** (a) Absolute uncertainty from use of different surrounding grid area for each spatial element
 1110 of our inversion domain in the sensitivity tests; 2° to 4° grid-cells were considered resulting in a mean
 1111 relative uncertainty of 4%. (b) Absolute uncertainty from use of four different prior emission
 1112 estimates, namely EC6G4, VD, EGG and NE (see section 2.3). Here, a much larger uncertainty was
 1113 calculated, due to the use of tenfold different prior emission datasets. (c) Propagated absolute
 1114 uncertainty from the different sensitivity tests, and (d) relative uncertainty with respect to the posterior
 1115 emissions (**Figure 2c**). The average uncertainty in the inversion domain for the first half of 2020 was
 1116 estimated to be 66%.

1117

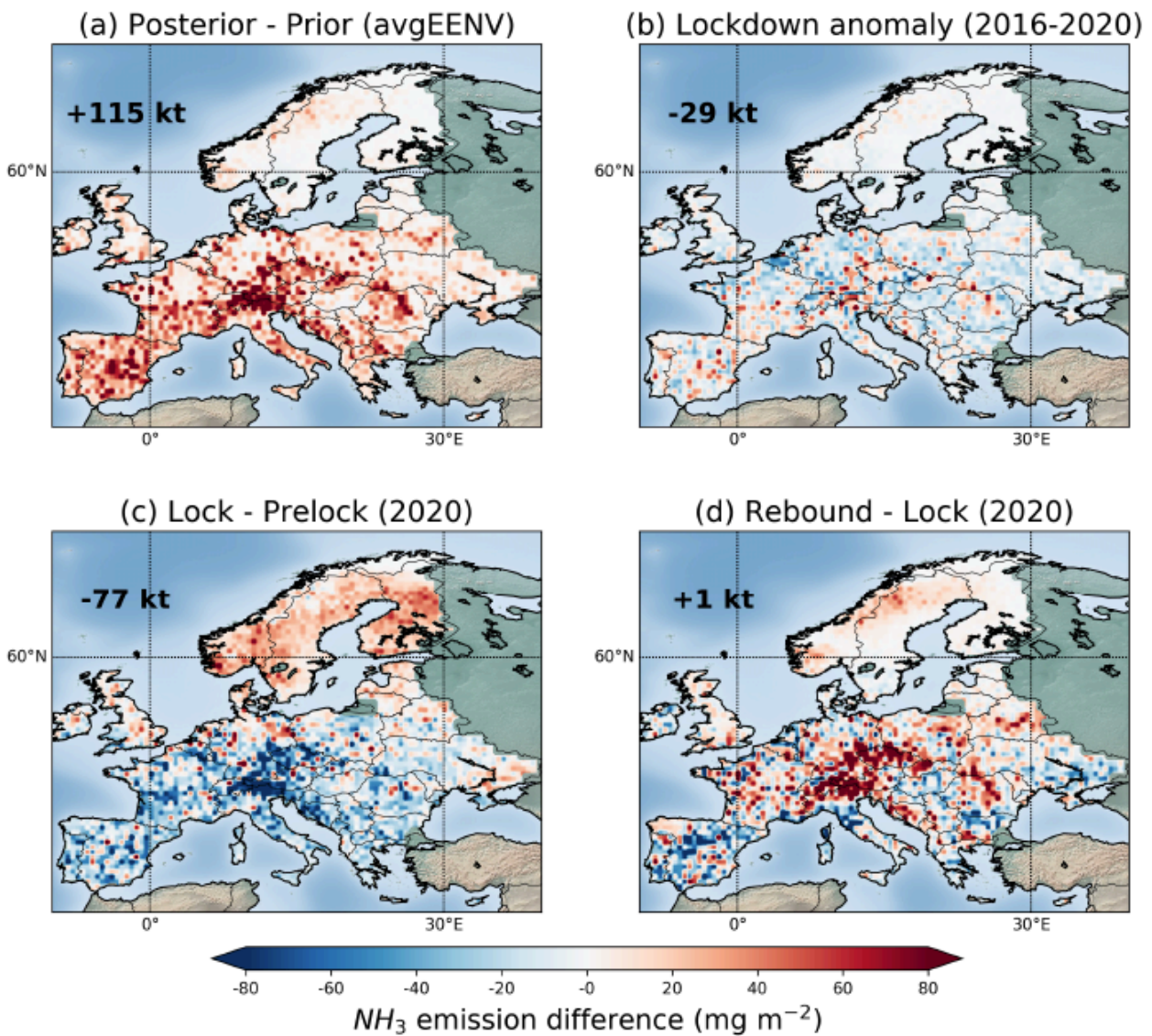


1118

1119 **Figure 4.** Timeseries of weekly-average posterior emissions of ammonia with the calculated
 1120 uncertainties in different European countries in 2020 resulting from inversions using prior
 1121 information from avgEENV plotted together with the CrIS observations averaged over Europe (red
 1122 line) and mean emissions with the calculated standard deviations for the reference period (2016–
 1123 2019). The single top numbers show the change in ammonia emissions during the 2020 lockdowns
 1124 (15 March – 30 April) as compared to the same period the years before (2016-2019), whereas the two
 1125 bottom ones show the respective changes in ammonia emissions during the 2020 lockdown
 1126 as compared to the period before the lockdown, and after lockdown finished compared to the lockdown
 1127 period (rebound period).

1128

1129

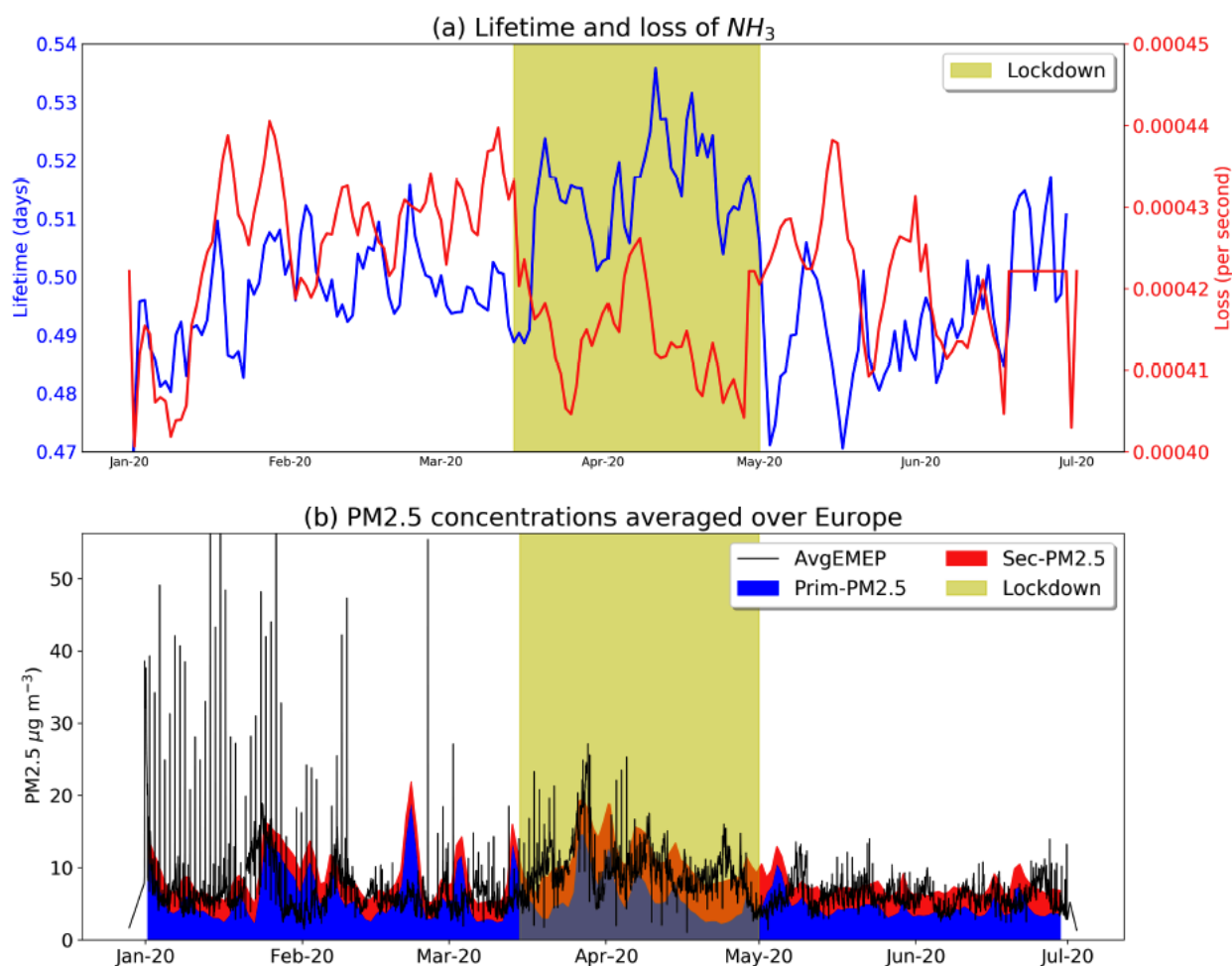


1130

1131 **Figure 5.** (a) Difference of posterior from prior emissions of ammonia during the European
 1132 lockdowns of 2020 (15 March – 30 April) using the avgEENV emissions as the prior. (b) Emission
 1133 anomaly relative to the 2020 lockdowns from the 2016-2020 period (15 March – 30 April).
 1134 Difference in posterior ammonia (c) during the 2020 lockdowns (15 March – 30 April, Lock) from
 1135 the period before (1 January – 14 March) and (d) after the 2020 lockdowns (1 May – 31 June, Reb)
 1136 from the period during the 2020 lockdowns (15 March – 30 April, Lock) compared with the
 1137 reference years (2016–2019).

1138

1139



1141

1142 **Figure 6.** (a) Modelled lifetime (blue) and loss-rates (red) of atmospheric ammonia averaged over
 1143 Europe for January – June 2020. The lockdown period (15 March – 30 April) is shaded in yellow.
 1144 Right after COVID-19 restrictions were applied, loss-rates of ammonia (shown in red) were
 1145 disturbed due to reported decreases on SO_2 and NO_x (Guevara et al., 2021; Doumbia et al., 2021),
 1146 precursors of sulfuric and nitric acids (with which ammonia reacts to form $PM_{2.5}$) and the constant
 1147 accumulation of atmospheric ammonia. This had an effect on the lifetime of ammonia (plotted in
 1148 blue), which started increasing in Europe leading to further accumulation of ammonia. (b)
 1149 Observations of $PM_{2.5}$ from the EMEP stations (78 stations) plotted against modelled $PM_{2.5}$
 1150 concentrations, both averaged over Europe, from primary sources and secondary formation. It is
 1151 evident that right after lockdown (yellow shade), secondary $PM_{2.5}$ formation maintained high
 1152 concentrations across Europe.

1153

1202

1203 **Figure S 7.** Modelled concentrations of PM_{2.5} against ground-based observations from EMEP
1204 stations for January to June 2020 presented in a Taylor diagram. The diagram shows the Pearson's
1205 correlation coefficient (gauging similarity in pattern between the modelled and observed
1206 concentrations) that is related to the azimuthal angle (blue contours); the standard deviation of
1207 modelled concentrations of ammonia is proportional to the radial distance from the origin (black
1208 contours) and the centered normalized RMSE of modelled concentrations is proportional to the
1209 distance from the reference standard deviation (green contours).

1210

1211 **Figure S 8.** Temperature (red) and specific humidity (blue) spatially averaged over Europe and
1212 vertically averaged up to 32 km (795 mbars) from ERA5 (Hersbach et al., 2020) for January – June
1213 2020. The lockdown period is shaded in grey.